Ocean Bottom Seismometer Clock Correction using Ambient Seismic Noise

Naranjo, David; Parisi, Laura; Jónsson, Sigurjón; Jousset, Philippe; Werthmüller, Dieter; Weemstra, Cornelis

Important note
To cite this publication, please use the final published version (if applicable).
Please check the document version above.

Ocean bottom seismometer clock correction using ambient seismic noise

David Naranjo [*,1,2], Laura Parisi [2], Sigurjón Jónsson [2], Philippe Jousset [3], Dieter Werthmüller [1], Cornelis Weemstra [1,4]

[1]Department of Geoscience and Engineering, Delft University of Technology, Stevinweg 1, 2628 CN, Delft, the Netherlands, [2]Physical Science and Engineering Division, King Abdullah University of Science and Technology, Thuwal, Makkah 23955, Saudi Arabia, [3]GFZ German Research Centre for Geosciences, Helmholtz Centre Potsdam, Section 2.2 Geophysical Imaging, Potsdam, Germany, [4]Department of Seismology and Acoustics, Royal Netherlands Meteorological Institute, Utrechtseweg 297, 3730 AE, De Bilt, the Netherlands

Author contributions: *Conceptualization*: CW, DN. *Software*: DN, CW, DW. *Formal Analysis*: All authors. *Investigation*: All authors. *Writing - original draft*: DN. *Writing - Review & Editing*: All authors. *Data acquisition*: PJ.

Abstract Ocean-bottom seismometers (OBSs) are equipped with seismic sensors that record acoustic and seismic events at the seafloor. One critical parameter for obtaining accurate earthquake locations is the absolute time of the recorded seismic signals. It is, however, not possible to synchronize the internal clocks of the OBSs with a known reference time, as GNSS signals do not reach the sea bottom. We address this issue by introducing a new method to synchronize the clocks of large-scale OBS deployments. Similar to some previous approaches, our method leverages the theoretical time-symmetry of time-averaged cross-correlations of ambient seismic noise: broken time-symmetry is attributed to clock drift. A non-uniform surface wave illumination pattern, however, can also break the time-symmetry. Existing noise-based synchronization techniques usually ignore the latter, but we do address it by means of a weighted least-squares inversion (based on station-to-station distances). The weighted least-squares inversion mitigates the adverse effect of a non-uniform surface wave illumination on the time-symmetry. Furthermore, our method includes a unique feature: it estimates and corrects for an initial clock error introduced at the deployment time. This initial clock error can be attributed to either (i) a wrong initial time synchronization or (ii) the temperature shock during deployment. The methodology is implemented in an open-source Python package named `OCloC` and was tested with OBS recordings acquired around the Reykjanes peninsula, southwest Iceland. Our results indicate that all OBSs experienced a clock drift, and that a significant number of them were subject to an initial clock error at the deployment time. This study provides a substantial improvement in the inherent quality of OBS data, laying a solid foundation for more robust seismic data analysis.

Non-technical summary Ocean-bottom seismometers (OBSs) are instruments deployed on the seafloor, equipped with sensors to record seismic activity offshore. However, getting accurate information from these instruments is challenging because the internal clocks of the OBSs cannot be easily synchronized with a known reference time. In this study, we developed a new approach to synchronize the clocks of large-scale OBS deployments. Our approach uses cross-correlations of ambient seismic noise to detect errors in the timing of the sensor clocks. We implemented our methodology in the open-source Python package `OCloC` and tested it on data from a seismic network deployed offshore the Reykjanes peninsula, southwest Iceland. This new approach will aid in improving the accuracy of earthquake locations and imaging the crust and upper mantle.

1 Introduction

Over the past few decades, there has been an increase in the use of ocean-bottom seismometers (OBSs). OBS readings allow one to identify remarkable features such as undersea volcanic eruptions (Matsumoto et al., 2019) or seismic activity linked to tectonic strain and gas emissions through fault conduits (Tary et al., 2011). In particular, OBS readings are frequently used for imaging

of the crust and/or mantle (e.g., Dongmo Wamba et al., 2023). Despite these successes, a key challenge in using OBSs remains the accurate (time) synchronization of the instruments' recordings. In fact, most OBS clocks drift, meaning they do not run at the same rate as a reference clock. This issue might be overcome by using atomic clocks instead of the traditional microprocessor-compensated crystal oscillator clocks that most OBSs have (Gardner and Collins, 2012). This, however, would increase the inventory costs and power consumption, implying fewer instruments and less monitoring time,

---

*Corresponding author: d.f.naranjohernandez@tudelft.nl

respectively. If the network is not properly synchronized, the incorrectly timed recordings may result in biased earthquake locations and Earth structure models.

One simple approach to identify clock drift is to measure the time difference between the instrument's internal clock and a GNSS signal before deployment and after recovery. This time difference is commonly referred to as the instrument's 'skew'. Assuming the instrument's clock drifted at a linear rate, a time correction can then be applied (e.g., Geissler et al., 2010). The skew, however, is not always possible to retrieve (e.g., when the instrument's battery dies before recovery). For this reason, several authors have proposed alternative methods for correcting clock errors; many of these exploiting the presumed temporal stability of time-averaged cross-correlations of ambient seismic noise (e.g., Sens-Schönfelder, 2008; Loviknes et al., 2020; Hannemann et al., 2014; Jousset et al., 2013). These approaches, however, ignore errors that could arise if the initial synchronization with a GNSS signal is either lacking or erroneous, or if there is an "initial" clock error resulting from the temperature shock during deployment (Zhang et al., 2023).

In theory, time-averaged cross-correlations of recordings of ambient seismic noise (henceforth 'noise cross-correlations') result in a signal that is symmetric around $t = 0$ (e.g., Stehly et al., 2006). In fact, under favorable conditions, the signals at positive and negative time lag coincide with the medium's Green's function (between the positions of the two seismic stations) and its time reverse, respectively. As such, it is referred to as 'seismic interferometry' (SI) (Wapenaar and Fokkema, 2006). In practice, these conditions are often not entirely fulfilled. Notwithstanding, provided the illumination is sufficiently uniform, the operation of averaging noise cross-correlations over time still yields two interferometric surface wave responses: one at the positive and one at the negative time lag(s). Violation of the noise cross-correlations' time symmetry may indicate the presence of clock errors (e.g., Hannemann et al., 2014).

Currently, two distinct approaches use noise cross-correlations to detect and correct clock errors (Gouédard et al., 2014). The first approach is based on the presumed temporal stability of the noise cross-correlations (Hable et al., 2018; Loviknes et al., 2020). In this approach, cross-correlation functions (CCFs) of ambient noise are calculated over different periods. The drift is then estimated as the time shift that maximizes the Pearson correlation coefficient between each CCF and a reference correlation function (Hable et al., 2018). However, this method ignores the possibility of an initial clock error at the time of deployment due to a temperature shock during the OBS' descent to the ocean floor (Gardner and Collins, 2012; Zhang et al., 2023). The second approach exploits the above-mentioned time symmetry between the retrieved interferometric responses (Sens-Schönfelder, 2008; Weemstra et al., 2021). Contrary to the first approach, both direct surface wave arrivals (i.e., at positive and negative time lag(s) need to be retrieved successfully in this case. Low signal-to-noise ratios or stations that are too close to each other

(in terms of wavelength) prohibit this.

Although existing approaches for correcting clock errors have proven successful, a few challenges remain. First, the symmetry of ambient noise cross-correlation, while a valuable theoretical concept, is rarely realized in practice. A non-uniform illumination pattern may cause shifts in the arrival time of the interferometric responses with respect to the true arrival time (a challenge that is often overlooked). Second, current methods ignore the possibility of the aforementioned initial clock error during deployment. This clock error, introduced during the OBS' descent, is not expected given the mechanism causing clock drift (e.g., Shariat-Panahi et al., 2009), but it would nonetheless be good to rule out; in particular because the first approach mentioned above (Hable et al., 2018; Loviknes et al., 2020), does not allow such initial clock error to be detected. Finally, many of the current methods rely on land seismometers that are considered to be devoid of clock errors, ideally in the vicinity of the OBS deployment. This, however, will not be the case when the OBS network is located in oceanic regions far from the coast.

In this paper, we present a versatile method that addresses all these challenges. Our approach (i) uses a weighted least-squares inversion to minimize the detrimental effect of non-uniform illumination patterns, (ii) allows for a potential initial clock error at deployment time, and (iii) does not require land stations to be included in the network to synchronize the recordings. Regarding the third claim, although our approach allows the OBS network's recordings to be synchronized, the combined set of recordings cannot be synchronized with Coordinated Universal Time (UTC). To achieve that, a land station (with a UTC-synchronized clock) needs to be included in the network. The presented method is implemented in an open-source Python package named `OCloC` (OBS Clock Correction), which accompanies this paper. It combines the two aforementioned techniques for clock error detection (i.e., the one relying on the presumed temporal stability of noise cross-correlations and the one relying on their presumed time symmetry). Our method (and hence the package) is particularly useful in application to large-N seismic arrays.

To show the validity of our method, we use data from a seismic network deployed on and around the Reykjanes peninsula, SW Iceland (Jousset et al., 2020a). This seismic network was deployed in the context of the geothermal project IMAGE (Integrated Methods for Advanced Geothermal Exploration, see also Jousset et al., 2020b; Blanck et al., 2020). The data set used consists of recordings by 30 on-land stations and 17 OBSs (this is a subset of the stations used in Weemstra et al., 2021). In the following sections, we detail the theory underlying our approach (Section 2), discuss and exemplify the implementation of this theory (Section 3), present and discuss our findings (Section 4), and list the most important conclusions (Section 6). A more detailed description of the data is included in Section 3 (Section 3.1). In addition, a brief description of `OCloC` is given in this section (Section 3.3).

2 Theory

In this section, the theory is introduced step-wise. First, we briefly highlight the most important theoretical aspects of Seismic Interferometry (SI). Second, we introduce a model adequate for determining clock drift, which is an extension of the model introduced by Weemstra et al. (2021). Third, we introduce potential additional time shifts (i.e., in addition to clock drift) affecting the arrival times of the interferometric responses. Fourth, we describe how a single noise cross-correlation's drift, and deviation from symmetry, can be retrieved. Fifth, we present the matrix notation of the introduced model. Finally, we briefly describe two different inversion approaches.

2.1 Seismic interferometry

Early types of seismic interferometry (SI) were introduced to the geophysics community by Aki (1957) and Claerbout (1968). Over the last two decades, the theory underlying SI has been established (Lobkis and Weaver, 2001; Wapenaar and Fokkema, 2006; Snieder, 2004; Shapiro and Campillo, 2004), and the method has been exploited in numerous applications. Examples include subsurface characterization (Draganov et al., 2007; Jousset et al., 2016), reservoir monitoring (Sánchez-Pastor et al., 2019), and glaciology (Lindner et al., 2018). In this study, SI is used as an independent method to recover clock errors without needing skew measurements.

Applying SI to recordings of ambient seismic noise allows one to retrieve new seismic responses between pairs of stations by means of simple cross-correlations (Wapenaar and Fokkema, 2006; Stehly et al., 2006). Under specific conditions, the time-averaged cross-correlation contains the response to two 'virtual sources': one at negative lag times (usually referred to as the 'acausal part') and another at positive lag times (referred to as the 'causal part'), and with the virtual sources coinciding with the receiver locations. Time averaging is required to suppress spurious travel time delays that arise from constructive interference of signals coming from different sources. The time-averaged noise cross-correlation is proportional to the medium's Green's function if: (i) the noise sources illuminate the station pairs uniformly from all angles, (ii) the noise sources are uncorrelated, (iii) the medium is lossless, and (iv) sources have coinciding amplitude spectra (Wapenaar and Fokkema, 2006). Under these assumptions, the time-averaged cross-correlation of noise recorded by stations at $\mathbf{x}_i$ and $\mathbf{x}_j$, which we denote by $C_{i,j}(t)$, is proportional to the Green's function $G(\mathbf{x}_j, \mathbf{x}_i, t)$ and its time-reversed version, convolved with the autocorrelation of the signal emitted by the (noise) sources, i.e.,

$$C_{i,j}(t) \propto [G(\mathbf{x}_j, \mathbf{x}_i, t) + G(\mathbf{x}_j, \mathbf{x}_i, -t)] * P(t), \quad (1)$$

where $P(t)$ denotes the signal's autocorrelation generated by noise sources. In this study, we focus on the direct surface wave part of the Green's functions, ignoring the scattered signal. We refer to Wapenaar and

Fokkema (2006) and Halliday and Curtis (2008) for a more detailed discussion of the assumptions underlying SI.

2.2 A model to account for clock drift

When it comes to the recovery of clock errors, an essential feature of the noise cross-correlation is its presumed time symmetry: under the assumptions listed in the previous section, the direct surface waves in $C_{i,j}(t)$ arrive at time lags of equal magnitude but opposite signs (Figure 1a). A violation of this time symmetry, such as the one in Figure 1b, indicates the presence of clock errors. To infer these clock errors from noise cross-correlations, Weemstra et al. (2021, Section 4) recently introduced an appropriate model. These authors, however, did not include clock drift in their model as they assumed the instrumental clock errors to be time-independent (or constant). We extend the model introduced by Weemstra et al. (2021) to account for time-dependent clock errors such as clock drift.

Here we assume the (potential) OBS clock drift to be linear. This is based on the fact that (i) the drift rate should be steady at constant temperature and (ii) the ambient temperature tends to be rather stable in deep water (note that the drift rate at a certain temperature is dictated by the frequency of the quartz oscillators in seismic clocks; Shariat-Panahi et al., 2009). The validity of this assumption has been demonstrated for OBSs at larger depths in previous studies (Hable et al., 2018; Loviknes et al., 2020).

To estimate clock drift, we compute time-lapse cross-correlations $C_{i,j}(t, t^{(\mathrm{lps})})$, where $t^{(\mathrm{lps})}$ is the timing of the time-lapse cross-correlation. We refer to $C_{i,j}(t, t^{(\mathrm{lps})})$ as the 'lapse cross-correlation'. Note that $t^{(\mathrm{lps})}$ is the average time of all time windows contributing to the lapse cross-correlation. Therefore, $t^{(\mathrm{lps})}$ is not necessarily the time exactly in between the time of the first and last time window contributing to $C_{i,j}(t, t^{(\mathrm{lps})})$: in case the recordings by one of the two stations (or both) contain gaps, $t^{(\mathrm{lps})}$ may be skewed towards the beginning or end of the entire period over which individual cross-correlations are averaged.

For the considered linear parametrization, the time-dependent clock error of station i, denoted by $\delta t_i^{(\mathrm{ins})}$, is written as

$$\delta t_i^{(\mathrm{ins})}\left(t^{(\mathrm{lps})}\right) = a_i t^{(\mathrm{lps})} + b_i, \quad (2)$$

where $\delta t_i^{(\mathrm{ins})}$ is the clock error of station i at $t^{(\mathrm{lps})}$, $t^{(\mathrm{lps})}$ is the average time of the time-lapse cross-correlation, a_i is the clock drift rate of station i, and b_i is the incurred clock error of station i at $t^{(\mathrm{lps})} = 0$.

Note that $t^{(\mathrm{lps})}$ is a continuous variable and that it is conveniently (but arbitrarily) set to 0 at the 21st of August 2014. This is the approximate time of deployment of the OBSs considered in this study (the OBSs have been deployed over the course of a number of days around that date). Furthermore, $\delta t_i^{(\mathrm{ins})}$ is defined such that negative values imply that the recordings by station i are subject to a time delay. The rate at which the clock of station i is drifting is given by a_i, whereas b_i represents
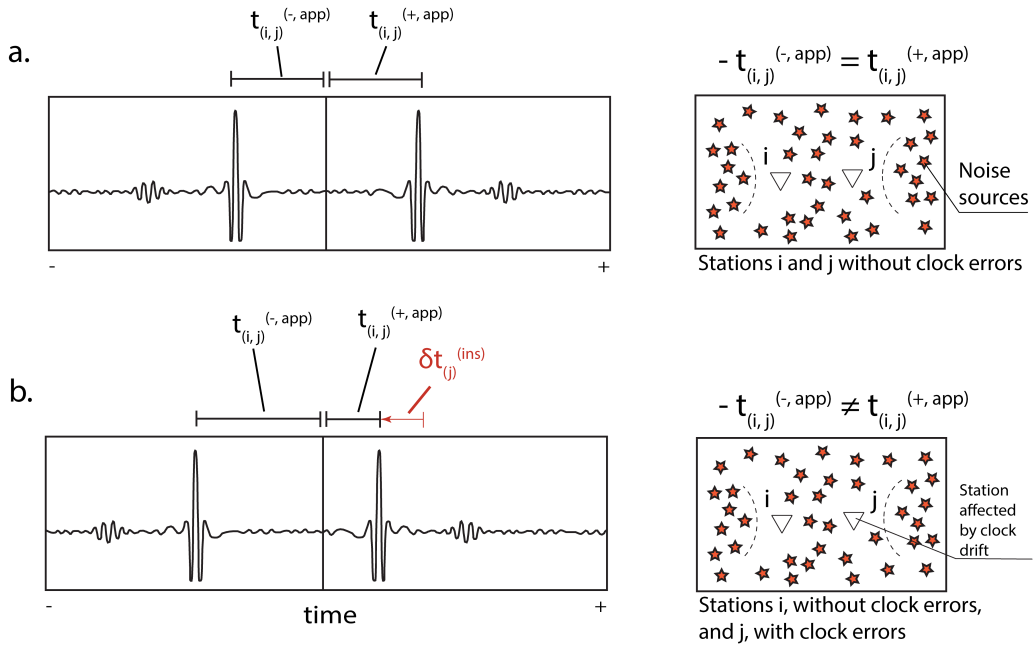
Figure 1 a. Noise cross-correlations computed using two stations without clock errors. The noise cross-correlation is almost symmetric in this case (for a relatively uniform illumination), and $t_{i,j}^{(+,\mathrm{app})} = -t_{i,j}^{(-,\mathrm{app})}$. b. Noise cross-correlations computed while one of the two stations is subject to clock errors (e.g., due to clock drift of one or both instruments). The noise cross-correlation is asymmetric (even for a relatively uniform illumination), and $t_{i,j}^{(+,\mathrm{app})} \neq -t_{i,j}^{(-,\mathrm{app})}$. In b, station j is subject to a clock error of $\delta t_j^{(\mathrm{ins})}$, which causes the noise cross-correlation to shift to negative time by that amount.

a possible clock error of station i at $t^{(\mathrm{lps})} = 0$. These are the two unknown parameters that we want to recover in this study (for all the OBSs). A different parametrization of $\delta t_i^{(\mathrm{ins})}$ in terms of, for example, cubic splines or trigonometric basis functions (i.e., Fourier series) is relatively straightforward.

A deviation from time symmetry can result from clock errors in either one or both stations involved in the noise cross-correlation. Similar to Weemstra et al. (2021), we denote the arrival time of the causal direct surface wave in $C_{i,j}(t, t^{(\mathrm{lps})})$ by $t_{i,j}^{(+,\mathrm{app})}$ and the arrival time of the acausal direct surface wave by $t_{i,j}^{(-,\mathrm{app})}$. Accounting for the time-dependent clock errors above, we obtain the following expression for the apparent arrival time of the causal direct surface wave:

$$t_{i,j}^{(+,\mathrm{app})}\left(t^{(\mathrm{lps})}\right) = t_{i,j}^{(+)} + \delta t_i^{(\mathrm{ins})}\left(t^{(\mathrm{lps})}\right) - \delta t_j^{(\mathrm{ins})}\left(t^{(\mathrm{lps})}\right). \tag{3}$$

Similarly, the apparent arrival time of the acausal direct surface wave is given by

$$t_{i,j}^{(-,\mathrm{app})}\left(t^{(\mathrm{lps})}\right) = t_{i,j}^{(-)} + \delta t_i^{(\mathrm{ins})}\left(t^{(\mathrm{lps})}\right) - \delta t_j^{(\mathrm{ins})}\left(t^{(\mathrm{lps})}\right). \tag{4}$$

Here, $t_{i,j}^{(+)}$ and $t_{i,j}^{(-)}$ are the true arrival times of the direct surface waves, i.e., the direct surface waves in $G(\mathbf{x}_j, \mathbf{x}_i, t)$ and $G(\mathbf{x}_j, \mathbf{x}_i, -t)$, respectively. Consequently, by definition, $t_{i,j}^{(+)} = -t_{i,j}^{(-)}$. It is useful to note that a temporal change in the medium (e.g. Lindner et al., 2018) does not affect the equality between $t_{i,j}^{(+)}$ and $-t_{i,j}^{(-)}$, as it merely modifies the Green's function.

Summing the left-hand and right-hand sides of equations (3) and (4), and subsequently substituting the linear parametrization defined in Equation (2), we find

$$\left(t_{i,j}^{(+,\mathrm{app})} + t_{i,j}^{(-,\mathrm{app})}\right)\left(t^{(\mathrm{lps})}\right)$$
$$= 2\delta t_i^{(\mathrm{ins})}\left(t^{(\mathrm{lps})}\right) - 2\delta t_j^{(\mathrm{ins})}\left(t^{(\mathrm{lps})}\right) \tag{5}$$
$$= 2a_i t^{(\mathrm{lps})} + 2b_i - 2a_j t^{(\mathrm{lps})} - 2b_j.$$

The variables here are shown schematically in Figure 1. In the ideal case that (i) the station couple is illuminated uniformly from all angles, (ii) spurious energy has effectively been stacked out in the time-averaging process, and (iii) the recordings are not subject to clock errors and/or drift, the right-hand side of Equation (5) evaluates to zero. If this is the case, then $t_{i,j}^{(+,app)} = -t_{i,j}^{(-,app)} = -t_{i,j}^{(-)} = t_{i,j}^{(+)}$. If, however, the measured $t_{i,j}^{(+,\mathrm{app})}$ and $t_{i,j}^{(-,\mathrm{app})}$ are such that the left-hand side of Equation (5) does not coincide with zero (and the aforementioned conditions are fulfilled), this indicates a clock error at either one or both stations. The associated broken time symmetry is illustrated in Figure 1b.

Assuming the number of lapse cross-correlations $N^{(\mathrm{lps})}$ to coincide for all cross-correlation pairs, $t^{(\mathrm{lps})}$ can be discretized as $t_k^{(\mathrm{lps})}$, where $k = 1, 2, \ldots, N^{(\mathrm{lps})}$. In that case, Equation (5) can be written as

$$t_{i,j,k}^{(+,\mathrm{app})} + t_{i,j,k}^{(-,\mathrm{app})} = 2a_i t_k^{(\mathrm{lps})} + 2b_i - 2a_j t_k^{(\mathrm{lps})} - 2b_j. \tag{6}$$

where the indices k in $t_{i,j,k}^{(+,\mathrm{app})}$ indicate that the arrival times of the direct surface waves are associated with

lapse time $t_k^{(\text{lps})}$. The procedure involving the determination of the $t_{i,j,k}^{(+,\text{app})} + t_{i,j,k}^{(-,\text{app})}$ is based on the study by Weemstra et al. (2021), and detailed in Section 2.4. The associated practical implementation is explained in Section 3.2. Finally, it is useful to note that we merely assume the number of lapse cross-correlations per station couple to coincide for notational convenience. In practice, both the number of lapse cross-correlations and their timing (i.e., the values of the $t_k^{(\text{lps})}$) may (and will) vary from one station couple to the other.

2.3   Additional arrival time shifts

Differences in amplitude between the causal and acausal arrivals occur if the noise intensity is larger in one stationary-phase direction than in the other (Stehly et al., 2006). Importantly, a non-uniform illumination pattern may also introduce (small) deviations, or time shifts, from the correct arrival time of the causal and acausal surface waves. We denote these additional time shifts by $\delta t_{i,j,k}^{(\text{src})}$ (the superscript 'src' implies that the time shift is associated with the source distribution). This time shift depends on all three indices since the (noise) illumination pattern usually varies as a function of both time (hence the index k) and station couple (hence the indices i and j). The time dependence of this term is due to the fact that the illumination pattern is usually non-stationary (e.g., Yang and Ritzwoller, 2008; Weemstra et al., 2013). The i, j dependence of this term is explained by the fact that the retrieved causal and acausal direct surface wave responses are associated with opposite stationary-phase regions (e.g., Snieder, 2004; Boschi and Weemstra, 2015). Azimuthal variations of the noise intensity in the two directions along the line connecting a station pair i and j, determine the magnitude of this arrival time shift. We therefore distinguish between $\delta t_{i,j,k}^{(+,\text{src})}$ and $\delta t_{i,j,k}^{(-,\text{src})}$, which represent (illumination related) arrival time shifts of the direct waves at positive (causal) and negative (acausal) time lag(s), respectively. In other words, the illumination-induced (additional) arrival time shifts of the causal and acausal direct surface waves can be expected to differ from each other (Weaver et al., 2009; Froment et al., 2010). We parenthetically note that the medium appears to be slower for a positive $\delta t_{i,j,k}^{(+,\text{src})}$, whereas a positive $\delta t_{i,j,k}^{(-,\text{src})}$ makes the medium appear to be faster than the actual medium.

In addition to the illumination-related arrival time shifts, we account for the presence of spurious energy by defining the additional time shifts $\delta t_{i,j,k}^{(+,\text{spur})}$ and $\delta t_{i,j,k}^{(-,\text{spur})}$, which, similar to $\delta t_{i,j,k}^{(+,\text{src})}$ and $\delta t_{i,j,k}^{(-,\text{src})}$, represent shifts in the arrival times of the causal and acausal direct surface waves, respectively (for details we refer to Weemstra et al., 2021). Including these time shifts in our model, Equation (6) reads:

$$
\begin{aligned}
t_{i,j,k}^{(+,\text{app})} & + t_{i,j,k}^{(-,\text{app})} \\
&= 2a_i t_k^{(\text{lps})} + 2b_i - 2a_j t_k^{(\text{lps})} - 2b_j \\
&\quad + \delta t_{i,j,k}^{(+,\text{src})} + \delta t_{i,j,k}^{(-,\text{src})} \\
&\quad + \delta t_{i,j,k}^{(+,\text{spur})} + \delta t_{i,j,k}^{(-,\text{spur})}. \qquad (7)
\end{aligned}
$$

2.4   Determination of $t_{i,j,k}^{(+,\text{app})} + t_{i,j,k}^{(-,\text{app})}$

As explained in Section 2.2, clock errors manifest themselves by breaking the time-symmetry of the lapse cross-correlations. In order to solve for a large number of a_i and b_i (i.e., to determine clock drift for large OBS arrays), time shifts of individual lapse cross-correlations need to be extracted in an automated fashion.

The $t_{i,j,k}^{(+,\text{app})} + t_{i,j,k}^{(-,\text{app})}$ (for all i, j, and k) are the entries of the data vector $\mathbf{t}^{(\text{app})}$. Our procedure starts by computing *a priori* estimates of these $t_{i,j,k}^{(+,\text{app})} + t_{i,j,k}^{(-,\text{app})}$. This estimate is based on the assumption that, for an individual station couple i, j, the drift accumulated over the interval from $t_1^{(\text{lps})}$ to $t_{N^{(\text{lps})}}^{(\text{lps})}$ is the combined result of a_i and a_j (i.e., that it is linear). Based on the presumed stability of both the medium and the noise illumination, the accumulated drift is estimated by cross-correlating the earliest lapse cross-correlation with the latest lapse cross-correlations: $(C_{i,j}(t, t_1^{(\text{lps})})$ is cross-correlated with $C_{i,j}(t, t_{N^{(\text{lps})}}^{(\text{lps})}))$. Assuming the drift to be linear and clock errors to coincide with zero at $t_k^{(\text{lps})} = 0$ then results in the sought-after *a priori* estimates of $t_{i,j,k}^{(+,\text{app})} + t_{i,j,k}^{(-,\text{app})}$, which we denote by $t_{i,j,k}^{(\text{a priori})}$. Note that, as such, the *a priori* estimate of $2b_i - 2b_j$ is assumed to be zero (see Equation 6). Clearly, this is a rather strong assumption. If an initial screening reveals that this assumption is not justified, it may be necessary to combine the procedure here with the procedure described in Section 5 of Weemstra et al. (2021). Finally, it is useful to note that instead of station-couple-specific *a priori* estimates, Weemstra et al. (2021) use station-specific *a priori* estimates to obtain $t_{i,j}^{(\text{a priori})}$ (without an index k because the analysis by Weemstra et al. (2021) does not account for clock drift, but merely allows one to determine time-independent clock errors).

The $t_{i,j,k}^{(\text{a priori})}$ are used to fill an initial estimate of the data vector $\mathbf{t}^{(\text{app})}$. By solving the inverse problem (explained below in Section 2.6), we recover *a priori* estimates of the a_i and b_i. As soon as these estimates are obtained, we apply the procedure described in Section 5 of Weemstra et al. (2021). In summary, this involves determining the time windows in which the causal and acausal direct surface waves are expected using (i) a reference surface wave velocity (which can be station-couple specific), (ii) the station-to-station distance, and (iii) *a priori* estimates of a_i and b_j. Knowing the approximate time windows in which the direct causal and acausal surface waves can be expected, the envelopes of the lapse cross-correlations are subsequently computed. The envelopes are used to determine the arrival time of the direct surface wave (either causal or acausal) with the largest amplitude difference between the top and bottom envelope (denoted by t^{est} in Weemstra et al., 2021). Finally, after interpolating the lapse cross-correlation for a time window (with a length of about one period) centered around the *a priori* estimates of $t_{i,j,k}^{(+,\text{app})}$ and $t_{i,j,k}^{(-,\text{app})}$, and cross-correlating the signals in these two-time windows, the desired measurement $t_{i,j,k}^{(+,\text{app})} + t_{i,j,k}^{(-,\text{app})}$ can be obtained. For a detailed description of the entire process, we refer to

1. Retrieve the crosscorrelations of each stationpair with the earliest and latest average date.

Earliest lapse crosscorrelation

$C_{i,j}(t, t_1^{(\mathrm{lps})})$

Latest lapse crosscorrelation

$C_{i,j}(t, t_{N^{(\mathrm{lps})}}^{(\mathrm{lps})})$
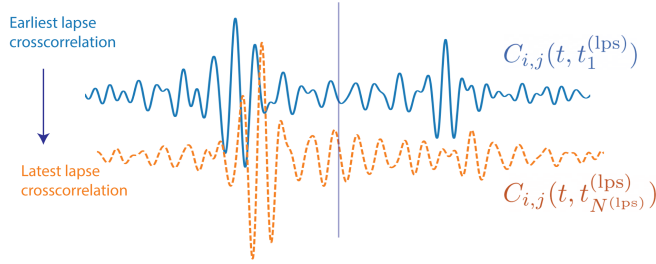
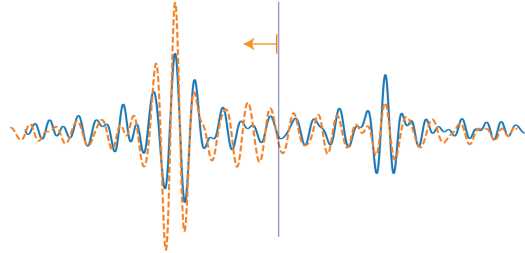2. Crosscorrelate both lapse crosscorrelations

Figure 2 Processing steps for calculating an *a priori* estimate of the combined clock drift of a given station pair.

Weemstra et al. (2021, Section 5).

2.5 Matrix formulation

Assuming we possess synchronous noise recordings by a total of N seismic stations and we compute a total of $N^{(\mathrm{lps})}$ lapse cross-correlations between each station pair, a maximum of $N^{(\mathrm{lps})}$ times $N(N-1)/2$ lapse cross-correlations can be obtained. The set of equations governing the $t_{i,j,k}^{(+,\mathrm{app})} + t_{i,j,k}^{(-,\mathrm{app})}$ can in that case be written as

$$\mathbf{A}\mathbf{t}^{(\mathrm{ins})} + \mathbf{n}^{(\mathrm{src})} + \mathbf{n}^{(\mathrm{spur})} = \mathbf{t}^{(\mathrm{app})}, \qquad (8)$$

where the vector $\mathbf{t}^{(\mathrm{ins})}$ contains the sought-for clock drift rates a_i and initial clock errors b_i. This vector has a length of $2N$. The rows of $\mathbf{A}$ relate to different station pairs and lapse times $t_k^{(\mathrm{lps})}$, i.e., they are associated with different $C_{i,j}\left(t, t_k^{(\mathrm{lps})}\right)$. Each column of $\mathbf{A}$ is associated with either an a_i or a b_i. Consequently, $\mathbf{A}$ has dimension $N^{(\mathrm{lps})}(N(N-1)/2) \times 2N$. The length of the vectors $\mathbf{t}^{(\mathrm{app})}$, $\mathbf{n}^{(\mathrm{src})}$, and $\mathbf{n}^{(\mathrm{spur})}$ obviously coincides with the number of rows of $\mathbf{A}$. The vector $\mathbf{t}^{(\mathrm{app})}$ contains the measurements and is often referred to as the 'data vector'. For the sake of clarity, we have detailed these vectors and matrices in Appendix A. Note that throughout this work, both matrices and vectors are indicated in bold; matrices are also capitalized, vectors not.

2.6 Inverting for clock drift

In the model introduced above, we considered the number of lapse cross-correlations $N^{(\mathrm{lps})}$ to coincide for all station pairs. In addition, we assumed these lapse cross-correlations to exist for all possible combinations of stations, i.e., $N(N-1)/2$. In application to field data however, $t^{(+,\mathrm{app})}$ and/or $t^{(-,\mathrm{app})}$ often cannot be determined for all lapse cross-correlations (i.e., all combinations of i, j and k). This implies that the number of

rows M of the matrix $\mathbf{A}$ (and hence the number of elements of $\mathbf{t}^{(\mathrm{app})}$, $\mathbf{n}^{(\mathrm{src})}$, and $\mathbf{n}^{(\mathrm{spur})}$) will in practice often be smaller than $N^{(\mathrm{lps})}N(N-1)/2$.

The inability to accurately determine $t^{(+,\mathrm{app})}$ and/or $t^{(-,\mathrm{app})}$ can be due to a number of reasons. First, if two stations are too close to each other with respect to the wavelengths considered, the direct surface-wave response at a positive time will overlap with the direct surface-wave response at a negative time. Second, the absence of sources in one of the two stationary phase directions will prevent the retrieval of the corresponding direct surface-wave response (e.g., Snieder, 2004). Clearly, this also prevents determining the associated arrival time. Third, gaps in the recordings by one or more stations may lead to fewer lapse cross-correlations.

Before we explain the two inversion approaches, we clarify the relation between matrix $\mathbf{A}$ and the ability to obtain a unique (least-squares) estimate of $\mathbf{t}^{(\mathrm{ins})}$. Because, as defined in Appendix A, the rank of $\mathbf{A}$ is two lower than the number of unknowns $2N$ (having a matrix with a rank that is lower than the number of unknowns is often referred to as 'rank deficient'). This indicates that the system of equations is effectively underdetermined. In other words, a unique estimate of $\mathbf{t}^{(\mathrm{ins})}$ does not exist for the system of equations defined in Equation (8). We distinguish between two cases: a land station is included in the network, or no land station is included in the network. In the first case, a unique estimate of $\mathbf{t}^{(\mathrm{ins})}$ exists if a number of conditions are fulfilled. We will detail these in the paragraph below. If the network consists solely of OBSs, a unique estimate of $\mathbf{t}^{(\mathrm{ins})}$ does not exist. We discuss that further below. Finally, an intuitive explanation of the rank deficiency is provided. Consider 10 lapse cross-correlations, each associated with a different $t_k^{(\mathrm{lps})}$ but with the same two OBSs. The matrix $\mathbf{A}$ would be a 10×4 matrix in that case (see Equation 6). Clearly, an infinite number of (least-

squares) solutions exist for b_1 and b_2 since adding any (arbitrary) value to both b_1 and b_2 would result in the same left-hand side. In other words, a unique solution for b_1 and b_2 does not exist. The same applies to a_1 and a_2.

In case a station with a UTC-synchronized clock is included in the network (i.e., a land station), the entries of that station can be eliminated from $\mathbf{t}^{(\mathrm{ins})}$ and the associated columns eliminated from $\mathbf{A}$ (see also the discussion in Section 6 and Appendix A in Weemstra et al., 2021). Subsequently, a number of conditions need to be fulfilled for a unique estimate of $\mathbf{t}^{(\mathrm{ins})}$ to exist. First, the system of equations (as defined in Equation 8) needs to contain at least two lines associated with lapse cross-correlations involving that station. These two lapse cross-correlations should be associated with a different lapse time $t_k^{(\mathrm{lps})}$. The land station in the first of the (at least) two lapse cross-correlations may, in fact, be a different land station from the land station associated with the second lapse cross-correlation, as long as the two lapse cross-correlations are associated with different $t_k^{(\mathrm{lps})}$. Second, each of the OBSs needs to be "part of" at least two lapse cross-correlations: there need to be two rows in $\mathbf{A}$ for which the entries associated with that OBS are non-zero. And again, these entries should be associated with different $t_k^{(\mathrm{lps})}$. In case these two conditions are fulfilled, the rank of $\mathbf{A}$ coincides with the number of unknowns ($2N$), and a unique least-squares estimate of the a_i and b_i in $\mathbf{t}^{(\mathrm{ins})}$ exists. Finally, the larger the difference in time between the various lapse cross-correlations of an OBS, the more accurate the estimates of its a_i and b_i.

If the network consists solely of OBSs, a unique estimate of $\mathbf{t}^{(\mathrm{ins})}$ does not exist. In that case, that least-squares estimate of $\mathbf{t}^{(\mathrm{ins})}$ is chosen that has the lowest norm, i.e., that minimizes $||\tilde{\mathbf{t}}^{(\mathrm{ins})}||$, where $\tilde{\mathbf{t}}^{(\mathrm{ins})}$ is any least-squares solution (or *least-squares estimator*) of the underdetermined system of equations. This solution is usually referred to as the *minimum norm* solution. The second condition above, which needed to be fulfilled to obtain a unique estimate of $\mathbf{t}^{(\mathrm{ins})}$, still applies in this case. That is, each of the OBSs still needs to be "part of" at least two lapse cross-correlations. The minimum-norm solution yields an estimator of $\mathbf{t}^{(\mathrm{ins})}$ that allows the OBS recordings to be synchronized with respect to each other, but not with respect to UTC. This is of course, still useful as it would enable tomographic studies using only the OBSs or the localization of seismic events (earthquake hypocenters) below the OBS array.

We consider two estimators of $\mathbf{t}^{(\mathrm{ins})}$. These are the 'ordinary least-squares estimator' $\tilde{\mathbf{t}}^{(\mathrm{ins})}_{(\mathrm{ols})}$, and the 'weighted least-squares estimator' $\tilde{\mathbf{t}}^{(\mathrm{ins})}_{(\mathrm{wls})}$. We refer to Weemstra et al. (2021) for a detailed description (and derivation) of these estimators and will only provide a brief explanation of these two estimators here. The ordinary least-squares estimator minimizes the misfit function $||\mathbf{t}^{(\mathrm{app})} - \mathbf{A}\mathbf{t}^{(\mathrm{ins})}||$ and hence does not account for (potential) variations in the $\delta t_{i,j,k}^{(\mathrm{src})}$ and/or $\delta t_{i,j,k}^{(\mathrm{spur})}$ for different i, j, k. The weighted least-squares estimator, instead, exploits the inverse proportionality of the illumination-

related arrival time shifts (i.e., the inverse proportionality of $\delta t_{i,j,k}^{(\mathrm{src})}$) to the true station-to-station travel time $t_{i,j}$ (as derived by Weaver et al., 2009). But since this travel time is usually not known, it uses the station-to-station distances $|\mathbf{x}_j - \mathbf{x}_i|$ as a proxy for the $t_{i,j}$. Measurements (i.e., individual $t_{i,j,k}^{(+,\mathrm{app})} + t_{i,j,k}^{(-,\mathrm{app})}$) associated with lapse cross-correlations between stations (i and j) that are further apart are hence assigned larger weights in the inversion.

3 Implementation & application to data

In this section, we describe the workflow that allows the estimators of $\mathbf{t}^{(\mathrm{ins})}$ to be computed (Section 3.2). Although predominantly methodological aspects of the workflow are discussed (results are presented in Section 4), some examples with field data are shown. We therefore start by introducing the IMAGE's seismic network and its lapse cross-correlations (Section 3.1). After describing the workflow, we dedicate one subsection to our package OCloC (Section 3.3). We finish this section with a description of a bootstrapping procedure that allows the stability of the recovered clock drift values to be assessed (Section 3.4).

3.1 The IMAGE data set

For heuristic purposes, the explanation of some processing steps of our workflow includes these steps' application to a set of lapse cross-correlations. These lapse cross-correlations are retrieved from recordings of ambient seismic noise acquired on and around the Reykjanes peninsula, SW Iceland (Jousset et al., 2020a). It concerns lapse cross-correlations between a subset of the stations considered by Weemstra et al. (2021). Specifically, about one year of noise recorded by 30 land stations and 17 OBSs is used (see Figure 3 for the station locations). The OBSs in this experiment are equipped with Seascan clocks (SEASCAN microcomputer compensated crystal oscillators), which are temperature-compensated.

The lapse cross-correlations are computed by averaging individual station-to-station cross-correlations over a 100-day period. These individual cross-correlations are computed per hour with a 50% overlap. We refer to Weemstra et al. (2021) for a detailed description of the computation of the hourly cross-correlations. Averaging individual (hourly) cross-correlations is performed in a two-step process. First, daily cross-correlations are computed based on a maximum of 47 hourly cross-correlations ($24 \times 2 - 1$). Subsequently, these daily cross-correlations are averaged. Importantly, gaps in the recordings by one or both stations are accounted for in the sense that the timing of a lapse cross-correlation, i.e., its $t_k^{(\mathrm{lps})}$, is defined as the average time of the individual cross-correlations. Gaps in the data can cause the average time of the correlations ($t_k^{(\mathrm{lps})}$) to deviate from the center of the 100-day period. Note that the $t_k^{(\mathrm{lps})}$ are allowed to differ between different station couples, as they are explicitly included in $\mathbf{A}$ (see also
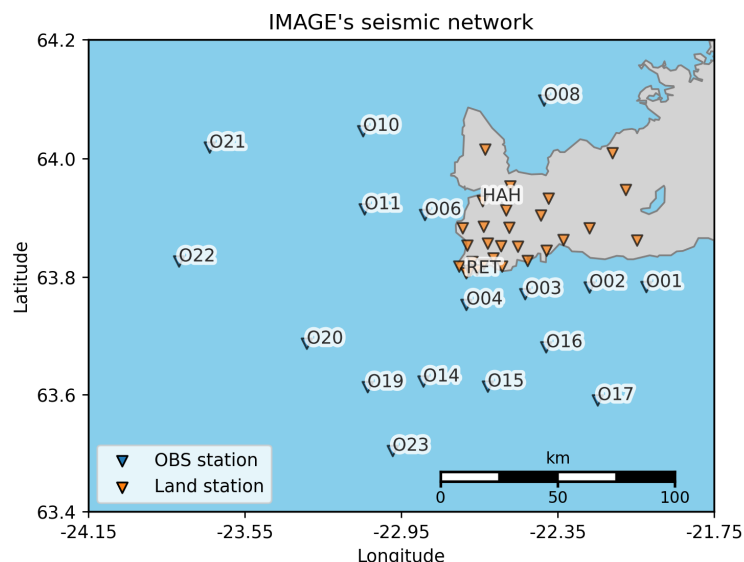
Figure 3 On-and off-shore stations of IMAGE's seismic network, SW Iceland, whose lapse cross-correlations were used in this study. Note that the numbering of the OBSs runs up to 23, whereas only 17 OBSs are included in our set of lapse cross-correlations (some stations did not sample the ambient seismic field sufficiently long and were hence excluded from our analysis; see also Figure S1 in Weemstra et al. (2021)). Only the land stations 'HAH' and 'RET', which are analyzed in Sections 3.2.5 and 4, are labeled due to space constraints.

Appendix A). In case the number of individual cross-correlations contributing to a lapse cross-correlation does not exceed 75% of the maximum number of individual cross-correlations (which is 100×47), that lapse cross-correlation is discarded. An overview of the data availability is given in Figure S1 of Weemstra et al. (2021).

3.2 Workflow

To determine and correct clock drift using lapse cross-correlations of ambient seismic noise, we adopt the processing sequence in Figure 4. It is this workflow that is implemented in OCloC. The workflow comprises five steps. We now dedicate one subsection to explain and discuss each of these steps.

3.2.1 Initial screening

In Figure 5a, all stations and ray paths associated with the available lapse cross-correlations are shown. To get a first impression of whether or not the OBS recordings are subject to clock drift, one can plot the different lapse cross-correlations in a single plot (i.e., time-averaged cross-correlations associated with different $t_k^{(\mathrm{lps})}$). In Figure 5b, we depict lapse cross-correlations between stations 020 and HAH (land station) for 5 different lapse times. Potential clock drift of an OBS manifests itself as a shift in time of the lapse cross-correlations: for this specific station couple, the lapse cross-correlations associated with larger $t_k^{(\mathrm{lps})}$ are shifted to a later time.

Prior to the determination of clock drift, it is important to choose an adequate bandpass filter. For the IMAGE data, the surface waves in the retrieved interferometric responses have the highest signal-to-noise ratios (SNRs) between 0.1 and 0.4 Hz. In general, however, the

Processing step	Methods
1. Initial screening	Bandpass filtering
2. Selecting eligible cross-correlations	Selection of SNR and distance thresholds
3. Determination of the $t_{i,j,k}^{(+,\mathrm{app})} + t_{i,j,k}^{(-,\mathrm{app})}$	Filtering out stations without enough station-connections / periods
4. Solving the inverse problem	Computation of the desired least-squares estimator
5. An iterative approach	Improving the estimation of $t_{i,j,k}^{(+,\mathrm{app})} + t_{i,j,k}^{(-,\mathrm{app})}$ by performing iterative inversions
6. Qualitative uncertainty analysis	Bootstrap re-sampling

Figure 4 Workflow for the determination of OBS clock drift using lapse cross-correlations of ambient seismic noise between a large number of OBSs (computed from large-N ocean-bottom seismometer deployments).

pass band depends on parameters such as the nominal station-to-station distance, the amplitude of the noise sources, the illumination pattern, and the geographical location of the OBS array (e.g., Yang and Ritzwoller, 2008). Note that, due to surface-wave dispersion, lower frequency bands usually result in smaller separations in time of the causal and acausal surface wave peaks.
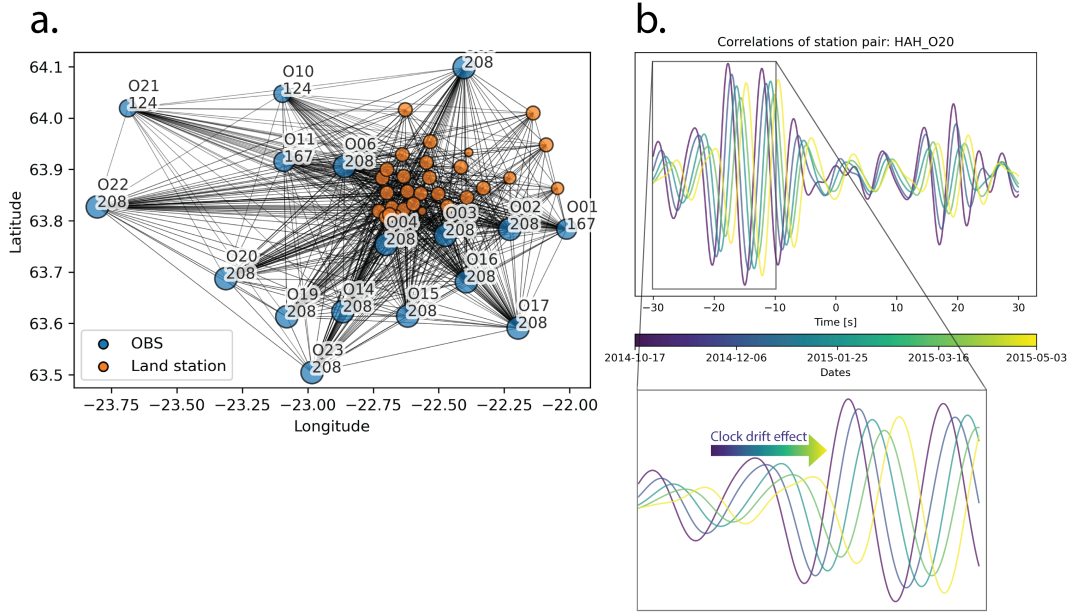
Figure 5 a. All seismic stations and ray paths; blue and orange circles correspond to OBSs and land seismometers, respectively. Only the station names of the OBSs are indicated. Below each station name, the number of available lapse cross-correlations involving that specific station is depicted. b. All lapse cross-correlations for a given station pair. The colors indicate the average timing ($t_k^{(\mathrm{lps})}$) of the lapse cross-correlation.

Importantly, the choice of frequency band also strongly affects the capability to determine the $t_{i,j,k}^{(+,\mathrm{app})} + t_{i,j,k}^{(-,\mathrm{app})}$ of individual lapse cross-correlations.

3.2.2 Selecting eligible lapse cross-correlations

There are two parameters that determine a lapse cross-correlation's eligibility to be included in the clock error estimation process: the SNR threshold and the station-to-station distance threshold. Together, these parameters determine which lapse cross-correlations are included in the inversion and which are not (i.e., whether their $t_{i,j,k}^{(+,\mathrm{app})} + t_{i,j,k}^{(-,\mathrm{app})}$ will be determined and added to data vector $\mathbf{t}^{(\mathrm{app})}$ or not).

In general, the quality of the measurements (i.e., the $t_{i,j,k}^{(+,\mathrm{app})} + t_{i,j,k}^{(-,\mathrm{app})}$) strongly depends on the signal-to-noise ratio (SNR). If the SNR is too low, the algorithm experiences difficulties determining the arrival times of the interferometric responses. Low SNRs are mainly due to low-intensity illumination from (one of) the stationary-phase regions (Snieder, 2004; Weaver et al., 2009). Consequently, the measurements may be inaccurate, or even subject to cycle skipping (Weemstra et al., 2021). Obviously, inaccurate entries in the data vector $\mathbf{t}^{(\mathrm{app})}$ (i.e., inaccurate $t_{i,j,k}^{(+,\mathrm{app})} + t_{i,j,k}^{(-,\mathrm{app})}$) adversely affect the inversion results. A clear example is shown in Figure 6a, where the causal peaks of the lapse cross-correlations between stations O08 and O21 have low SNRs. In this case, the determination of the arrival time of the causal peak is not straightforward and hence may result in inaccurate $t_{i,j,k}^{(+,\mathrm{app})} + t_{i,j,k}^{(-,\mathrm{app})}$. Both SNRs, of the causal and acausal interferometric direct surface waves, need to exceed the SNR threshold for the lapse cross-correlations to be included in the inversion. For details regarding the computation of the SNR, we refer

to Weemstra et al. (2021).

The second important parameter when it comes to the accuracy of the $t_{i,j,k}^{(+,\mathrm{app})} + t_{i,j,k}^{(-,\mathrm{app})}$ is the station-to-station distance. If two stations are too close to each other, the direct surface-wave response at a positive time (i.e., the causal arrival) will overlap with the direct surface-wave response at a negative time (i.e., the acausal arrival). Consequently, our algorithm will simply not be able to correctly determine the $t_{i,j,k}^{(+,\mathrm{app})} + t_{i,j,k}^{(-,\mathrm{app})}$ for those station couples. To prevent the inclusion of such measurements in the system of equations, the user must set a station-to-station distance threshold. This threshold is expressed in terms of wavelengths since the ability to distinguish the causal from the acausal arrival does not merely depend on the surface wave travel time, but on the ratio between the travel time and the (dominant) period of the interferometric surface waves. This threshold needs to be set at the start of the workflow (for further details regarding the station-to-station distance threshold we refer to Weemstra et al., 2021). A lapse cross-correlation's station-to-station distance needs to exceed the distance threshold for that lapse cross-correlation to be included in the inversion (i.e., for the $t_{i,j,k}^{(+,\mathrm{app})} + t_{i,j,k}^{(-,\mathrm{app})}$ to be determined and added to data vector $\mathbf{t}^{(\mathrm{app})}$).

Using the IMAGE lapse cross-correlations, we investigate how different thresholds affect the number of eligible lapse cross-correlations. If the thresholds are set too high, there will not be sufficient lapse cross-correlations to (accurately) determine the clock drift of all OBSs (i.e., the vector $\mathbf{t}^{(\mathrm{app})}$ will be relatively short). Conversely, if the thresholds are too low, we add too many inaccurate data points to the data vector, in turn leading to less accurate a_i and b_i (and hence less accu-
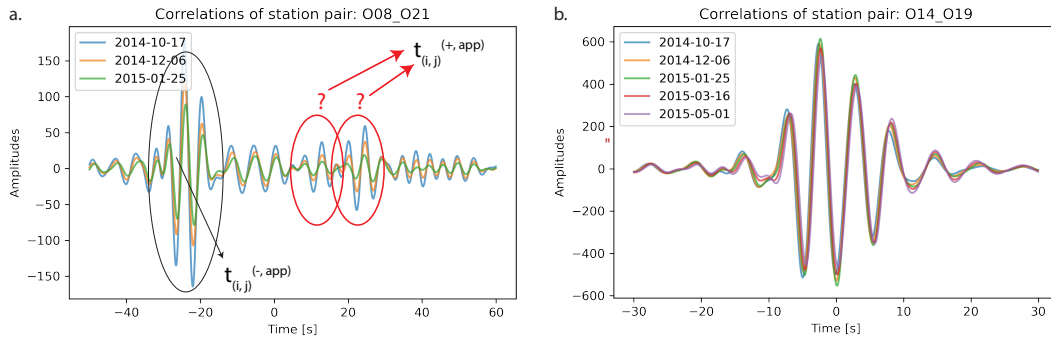
Figure 6 a. Lapse cross-correlations between OBSs O08 and O21: the signal-to-noise ratio of the causal wave is rather low, complicating the determination of $t_{i,j,k}^{(+,\text{app})} + t_{i,j,k}^{(-,\text{app})}$. b. Lapse cross-correlations between stations O14 and O19: The station-to-station distance of these stations is so small (10.6 km) that the causal and acausal surface waves overlap (note that for surface waves with a period of 5 seconds that propagate at 3000 m/s, 10.6 km corresponds to only 2/3 of a wavelength).

rate clock drift estimates). Figure 7 depicts the number of eligible station pairs exceeding a specific combination of thresholds. Obviously, lower thresholds result in a higher number of eligible lapse cross-correlations. Although a higher number of lapse cross-correlations implies a larger number of measurements, it has been shown that station-to-station distance thresholds in the range of 2 to 4 wavelengths and SNR thresholds of about 15 yield the most accurate clock errors (Weemstra et al., 2021). The latter values, however, are based on synthetic data. Here, we therefore choose a slightly more conservative SNR threshold of 30, while setting the station-to-station distance threshold to 2.5. The lapse cross-correlations fulfilling these criteria (i.e., exceeding these thresholds) are added to $\mathbf{t}^{(\text{app})}$ and hence enter the inversion.
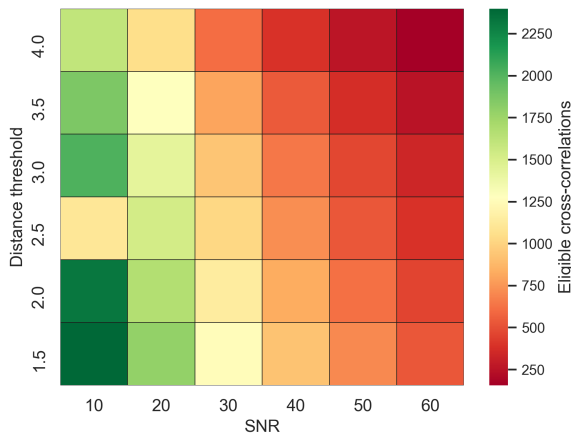

Figure 7 Number of eligible lapse cross-correlations for different station-to-station distances and SNR thresholds.

3.2.3 Determination of the $t_{i,j,k}^{(+,\text{app})} + t_{i,j,k}^{(-,\text{app})}$ for all selected combinations i, j, k

Although the calculation of $t_{i,j,k}^{(+,\text{app})} + t_{i,j,k}^{(-,\text{app})}$ is explained in Section 2.4, a few "practicalities" require attention. First, the algorithm computes the aforementioned *a priori* clock drift estimate only for lapse cross-correlations that exceed the SNR and station-to-station

distance thresholds. This may result in some stations having few unique "connections" with other stations. It may be better to, for each station, set both a minimum number of unique connections and a minimum number of total lapse cross-correlations. The lapse cross-correlations, associated with a station that does not exceed these thresholds, will be eliminated from the system of equations (i.e., the data vector $\mathbf{t}^{(\text{app})}$ will be shortened, and the number of rows and columns of the matrix $\mathbf{A}$ decreases).

Second, to recover a unique estimate of a station's clock drift (i.e., of the a_i), that station needs to be associated with lapse cross-correlations at various lapse times $t_k^{(\text{lps})}$ (recall the discussion in Section 2.6). In other words, $t_{i,j,k}^{(+,app)} + t_{i,j,k}^{(-,app)}$ needs to have been determined for various k for that station. By defining (i) a minimum number of correlation periods, (ii) the number of different lapse times required, and (iii) the minimum separation in days between an OBS' lapse cross-correlations, a unique solution can be guaranteed (i.e., provided lapse cross-correlations involving a land station are present, the system of equations will then not be rank deficient). These parameters can be set in OCloC.

Finally, a notorious problem in the inversion is what has been referred to as "cycle skipping" by Weemstra et al. (2021). That is, a measurement deviates from the true $t_{i,j,k}^{(+,\text{app})} + t_{i,j,k}^{(-,\text{app})}$ by approximately one period. Needless to say, the inclusion of these measurements in the inversion leads to incorrect a_i and b_i. In Appendix B, we describe a procedure allowing one to detect such outliers and discard them.

3.2.4 Solving the inverse problem

As mentioned in Section 2.6, two inversion strategies can be adopted (both implemented in OCloC): the ordinary least squares estimator $\tilde{\mathbf{t}}_{(\text{ols})}^{(\text{ins})}$ and the weighted least-squares estimator $\tilde{\mathbf{t}}_{(\text{wls})}^{(\text{ins})}$ can be computed. The ordinary least-squares estimator can be used if the noise sources uniformly illuminate the stations from all directions. In that case, the vector $\mathbf{n}^{(\text{src})}$ in Equation (8) coincides with $\mathbf{0}$ and the only source of noise is $\mathbf{n}^{(\text{spur})}$. Assuming the entries of the latter vector to have coinciding variance, the ordinary least-squares estimator $\tilde{\mathbf{t}}_{(\text{ols})}^{(\text{ins})}$

will give the most accurate estimate of $\mathbf{t}^{(\text{ins})}$ (in a least-squares sense).

In case the surface wave illumination is not uniform (as is in practice often the case; Yang and Ritzwoller, 2008; Stehly et al., 2006), $\mathbf{n}^{(\text{src})}$ does not coincide with zero, and it is more appropriate to compute the weighted least-squares estimator $\tilde{\mathbf{t}}^{(\text{ins})}_{(\text{wls})}$, where the station-to-station distances $|\mathbf{x}_j - \mathbf{x}_i|$ act as weights (see Section 2.6, and, for further details, Weemstra et al., 2021). In Section 5.1, we demonstrate the superiority of the weighted least-squares estimator, which was previously shown using synthetic noise cross-correlations. Finally, in the absence of lapse cross-correlations with recordings by a land station, the minimum-norm solution is computed. In this case, the recovered b_i differs from the true (unknown) b_i by a common time shift.

3.2.5 An iterative approach

Upon solving the inverse problem using the *a priori* estimates $t^{(\text{a priori})}_{i,j,k}$, we obtain an initial estimate of the a_i and b_i values of each station. The latter can subsequently be used to improve the estimation of $t^{(+,\text{app})}_{i,j,k} + t^{(-,\text{app})}_{i,j,k}$ as they can be used to predict the arrival time of the interferometric surface wave responses (see also Weemstra et al., 2021). It is therefore recommended to perform several inversions, each iteration using the previously obtained a_i and b_i to guide the estimation of the $t^{(+,\text{app})}_{i,j,k} + t^{(-,\text{app})}_{i,j,k}$ resulting in an updated data vector $\mathbf{t}^{(\text{app})}$, until the recovered a_i and b_i do not change anymore. By simply plotting the evolution of the recovered a_i and b_i, it is possible to determine when this is the case.

By plotting all lapse cross-correlations associated with a single station couple in one frame, and doing this separately for the corrected (using the obtained a_i and b_i) and uncorrected set of lapse cross-correlations, a (qualitative) impression of the result is obtained. If the lapse cross-correlations associated with different lapse times align, then the clock drift is successfully removed. An example of a successful clock drift removal is shown in Figure 8. It is clear that the lapse cross-correlations suffered from clock drift of OBS O20 (Figure 8a). Once the clock drift is removed, the lapse cross-correlations associated with different lapse times nicely align, as shown in Figure 8b.

3.3 OCloC

The methodology presented in this paper has been implemented in OCloC. In particular, OCloC allows the workflow detailed in the previous subsection to be executed. OCloC is an open-source Python package that has been tested for the operating systems Linux and macOS. We chose Python as OCloC's main programming language for its open-source, versatile, and cross-platform compatible nature, which is widely used in the Earth sciences (e.g., Werthmüller et al., 2021; Rücker et al., 2017). In the case of OCloC, the portability of Python enabled us to outsource specific computational aspects to a pre-compiled Fortran module.
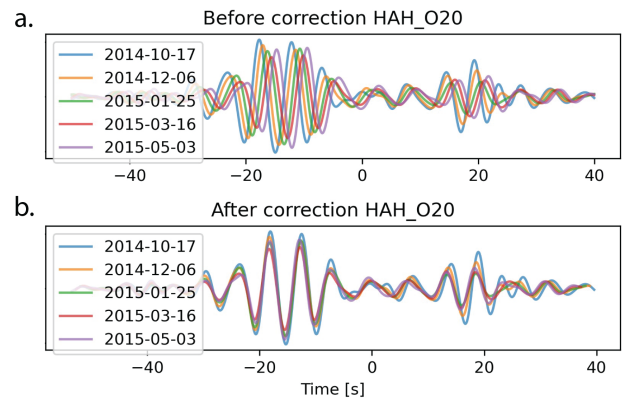

Figure 8 Lapse cross-correlations between land station HAH and OBS O20 for different lapse times. a. Cross-correlations before applying time corrections b. Lapse cross-correlations after correcting the clock drift of O20 using the a_i and b_i recovered by means of the iterative weighted least-squares inversion.

Through the application of seismic interferometry, the proposed correction of clock errors is contingent on the availability of synchronous noise recordings. The computation of the lapse cross-correlations, however, is deliberately left out of OCloC. The reason is that it will be nearly impossible to account for the plethora of different (pre-)processing approaches (Seats et al., 2012; Groos et al., 2012; Weemstra et al., 2014; Fichtner, 2014). This implies that users of the package have complete freedom regarding pre-processing (e.g., one-bit normalization, spectral whitening, etc.) and potential filter settings while computing the lapse cross-correlations, and that they are expected to do this themselves prior to the application of OCloC. The lapse cross-correlations can subsequently be imported as OCloC objects.

OCloC's functionality includes loading lapse cross-correlation files, storing and accessing station metadata, and solving the linear systems of equations in Section 2.5 in a (weighted) least-squares sense. It also has some other supporting functions. To keep the use of OCloC simple, a hierarchical object-oriented design has been adopted. This kind of architecture breaks down the whole process of determining and correcting clock errors into solvable chunks while letting the user know when an error occurred and how to prevent it.

The main object types of OCloC are: ClockDrift, ProcessingParameters, Correlation, and Station. Figure 9 depicts, schematically, the algorithm's object hierarchy. These objects need some clarification:

1. ClockDrift: The outermost layer of the hierarchical structure. The user deals with this object for the main processing steps described in Section 3.2. This object stores the different Station and Correlation objects in the form of lists. This object also stores the system of equations, described in Section 2, in the form of a Pandas dataframe (Wes McKinney, 2010a). The different methods of ClockDrift provide access to correlation files, station metadata, plotting functions, and different processing tools required for the algorithm's usage.
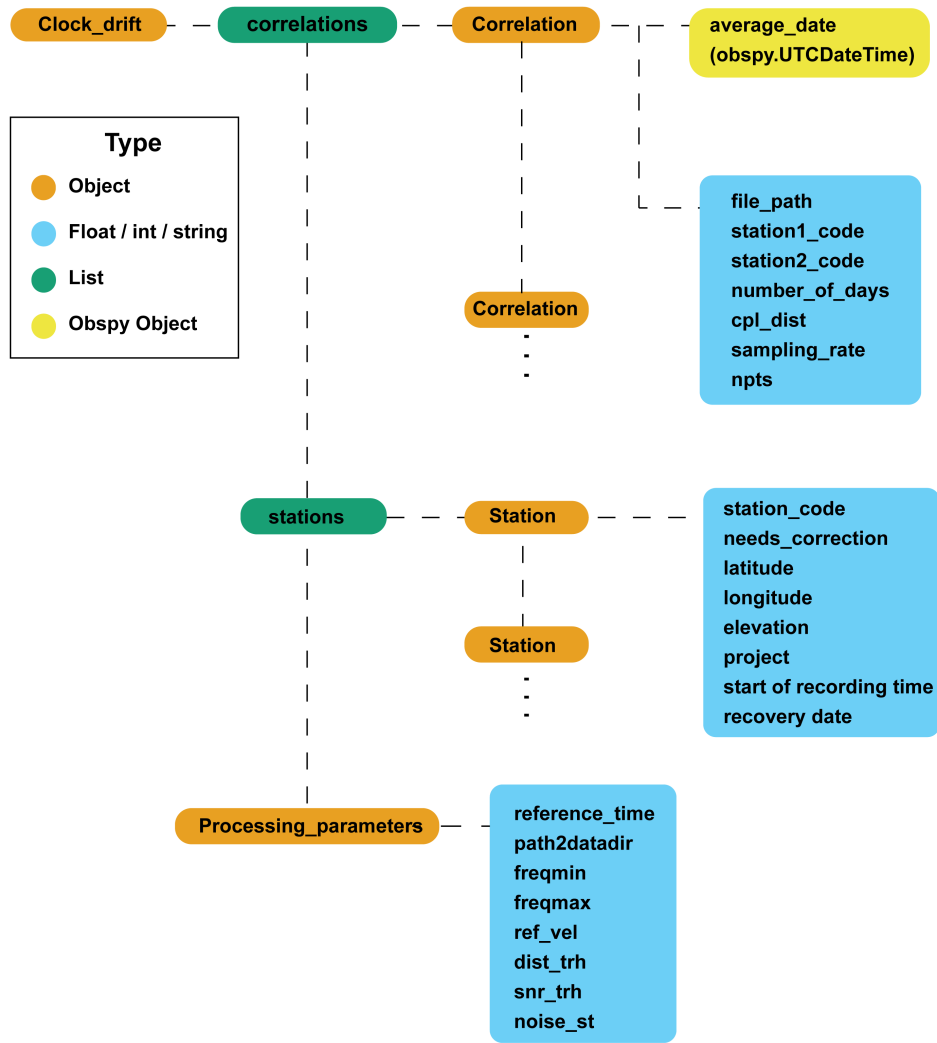
Figure 9 Object hierarchy of `OCloC`.

2. `ProcessingParameters`: The recovery of clock errors depends on the adequate selection of some pre-processing steps. `ProcessingParameters` object stores the value of these parameters. These parameters are the band-pass filter's corner frequencies, the SNR threshold, and the station-to-station distance threshold. These parameters are detailed in Section 3.2.

3. `Correlation`: Stores the metadata of each cross-correlation file such as the station names, the lapse time $t_k^{(lps)}$, and station-to-station distance, among others. Additionally, this object has functions to compute $t_{i,j,k}^{(+,\mathrm{app})} + t_{i,j,k}^{(-,\mathrm{app})}$, together with the signal-to-noise ratios of the causal and acausal surface wave arrivals.

4. `Station`: Contains metadata such as location, code, and timestamp when the station started recording. Moreover, after solving the linear system of equations, the recovered clock errors, i.e., the a_i and b_i, can be retrieved through these objects.

In addition to the core module, `OCloC` incorporates third-party dependencies that yield advanced function-

ality, namely, the Numpy programming library (Harris et al., 2020), several signal processing functions from Obspy (Krischer et al., 2015), and the data visualization tools of Pandas (Wes McKinney, 2010b) and Matplotlib (Hunter, 2007). For specific details regarding the package installation and usage, please refer to the online documentation available at https://ocloc.readthedocs.io.

3.4   Bootstrap re-sampling

To verify the robustness of the obtained results, we repeat the inversion several times using different sets of measurements $t_{i,j,k}^{(+,\mathrm{app})} + t_{i,j,k}^{(-,\mathrm{app})}$. By repeating the inversion multiple times, mean values and confidence intervals of the sought-after parameters are obtained. One way to artificially generate different sets of measurements is using bootstrap re-sampling (Efron, 1982). Bootstrapping is a statistical method that falls under the broader class of re-sampling methods. It allows one to estimate statistical properties of interest such as sample averages and variances (Schnaidt and Heinson, 2015). Effectively, it gives an indication of which results are likely and which are less likely without computing new lapse cross-correlations. Here, we seek to obtain an es-

timate of the variance of the estimated a_i and b_i. Instead of using all the measured data points, we sample with replacement (Efron, 1982, 1992). In practice, we generate a large number of data vectors $\mathbf{t}^{(\mathrm{app})}$ (usually referred to as 'realizations'), each with the same length as the original data vector, but with values that are drawn from the original data vector, allowing duplicates. Specifically, we perform the following steps:

I. An initial estimate of clock drift is obtained following steps one to five of Figure 4. A SNR threshold of 30 and a station-to-station distance threshold of 2.5 wavelengths are applied. It is necessary to check that the recovered a_i and b_i values are no longer changing after several iterations. This results in the data vector $\mathbf{t}^{(\mathrm{app})}$ that serves as the input of our bootstrapping procedure.

II. Allow sampling with replacement by randomly selecting measurements of $t_{i,j}^{(+,\mathrm{app})} + t_{i,j}^{(-,\mathrm{app})}$ (bootstrapped samples).

III. Once having re-sampled the measurements, perform the inversion and store the recovered a_i^* and b_i^* values of each station.

IV. Repeat steps II and III one thousand times. By doing so, we store 1000 possible realizations of the recovered a_i^* and b_i^* values.

V. Based on all the a_i^* and b_i^* realizations, compute a statistical measure, such as 95% confidence intervals, for each of the stations.

To identify stations with relatively uncertain a and b values (either due to a limited number of data points, or due to a lot of noise on the lapse cross-correlations associated with that specific station), we estimate the standard deviation and 95% confidence intervals (CI) from the 1000 realizations. The CI represents the range in which 95% of the a_i^* and b_i^* values lie.

The bootstrap approach allows one to identify OBSs with narrow or large confidence intervals. Narrower confidence intervals suggest the recovered a and b are well-determined, whereas stations with larger confidence intervals point to larger uncertainties in the recovered clock errors. In the absence of noise, i.e., $\mathbf{n}^{(\mathrm{src})}$ and $\mathbf{n}^{(\mathrm{spur})}$ both coinciding with $\mathbf{0}$, all a_i^* and b_i^* of a given station should coincide and hence the 95% confidence interval would be zero.

4 Results

4.1 Clock drift rates

We computed the weighted least-squares estimator of $\mathbf{t}^{(\mathrm{ins})}$ for the OBSs in the IMAGE's network. Our findings indicate that all OBS stations experienced clock drift. Compared to the other OBSs, the clock drift of OBS O20 was particularly large. Table 1 summarizes the estimated clock drift rates (i.e., the a_i) and incurred clock errors at the time of deployment. The latter may deviate slightly from the b_i because the b_i represents the clock errors on August 21, 2014 ($t^{(\mathrm{lps})} = 0$), whereas

most stations were not deployed exactly on that date. In addition, we list the measured skews in the last column. To compare these skew values, we provide in the fifth column the clock error at the time of recovery computed using the estimated a_i and b_i. Note that most OBS recordings end prior to that date due to full disks. We also obtained a drift estimate for OBS O21, which had no skew value documented due to a dead battery at the time of recovery. The incurred initial clock errors at the time of deployment ranged from a minimum of -0.404 s to a maximum of 0.037 s.

The bootstrap re-sampling introduced in Section 3.4 allows us to estimate the variance of the recovered a_i and b_i. By generating 1000 different data vectors (realizations) and subsequently performing a separate inversion for each of the generated data vectors, 1000 weighted least-squares estimators of $\mathbf{t}^{(\mathrm{ins})}$) are obtained. The standard deviation of the recovered a_i^* from the a_i (recovered using the original $\mathbf{t}^{(\mathrm{app})}$) is listed in column 3 of Table 1. In Figure 10, we visualize the recovered a_i and b_i, including the bootstrap-derived uncertainties.
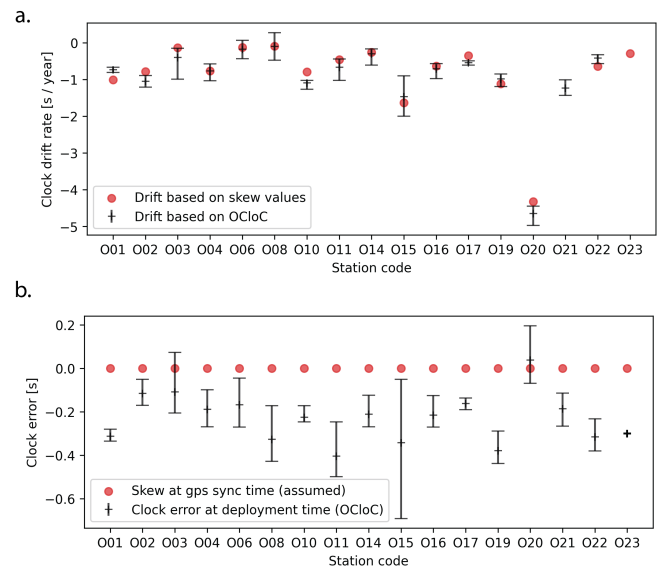

Figure 10 Comparison between clock drifts obtained in this study, and the measured skews. a. Comparison of clock drift rates estimated based on the skew values and the total recording time (red dots) and the a_i obtained from our weighted least-squares inversion (black crosses). The error bars correspond to the 95% confidence intervals resulting from the bootstrap re-sampling. Note that no skew value was reported for OBS O21 as this instrument's battery died before recovery. b. Comparison of the initial clock error at the OBS' deployment time. In both a and b, OBS O23 has no error bars as this OBS was associated with too few data points in $\mathbf{t}^{(\mathrm{app})}$ to be successfully included in the bootstrapping procedure.

For all station pairs, we plotted the waveform (mis)alignment of the different lapse cross-correlations to verify the effective removal of the clock errors. Figure 11 shows the time-lapse cross-correlations between OBS O01 and land station RET (which is devoid of clock errors) in three states: a) uncorrected, b) corrected

Table 1 Estimated clock drift rates (a_i) of the OBSs (2nd column), and their corresponding standard deviation (3rd column). The clock drift rates in column four are based on the measured skew values, assuming a linear drift and no clock errors at $t^{(\mathrm{lps})} = 0$. The estimated clock errors at deployment and recovery time in the fifth and sixth columns, respectively, are computed by substituting the estimated a_i and b_i in Equation (2) with $t^{(\mathrm{lps})}$ set to each OBS' day of deployment and recovery. OBS O21 had no skew value reported, as the battery died before recovery. Station O23 has no standard deviation because it was associated with too few data points in $\mathbf{t}^{(\mathrm{app})}$ to be successfully included in the bootstrapping procedure. This is probably due to the relatively low SNRs of the lapse cross-correlations involving this station.

Station name	Clock drift rate based on OCloC [s/year]	σ [s/year]	Clock drift rate based on skew values [s/year]	Clock error at deployment time (OCloC) [s]	Clock error at recovery time [s]	Measured skew [s]
O01	-0.734739	0.042760	-1.011740	-0.312892	-1.055899	-1.023125
O02	-1.055136	0.097011	-0.782087	-0.115908	-1.182942	-0.790906
O03	-0.401807	0.251438	-0.136396	-0.109015	-0.515270	-0.137906
O04	-0.770560	0.153252	-0.765888	-0.189565	-0.968726	-0.774437
O06	-0.172589	0.152249	-0.126476	-0.167177	-0.343849	-0.129468
O08	-0.104288	0.245437	-0.096861	-0.326683	-0.433947	-0.099625
O10	-1.095582	0.073045	-0.789557	-0.225825	-1.354066	-0.813093
O11	-0.667440	0.179920	-0.457559	-0.404513	-1.089599	-0.469656
O14	-0.304885	0.147440	-0.326255	-0.211671	-0.462262	-0.268156
O15	-1.465134	0.340357	-1.633493	-0.342048	-1.839114	-1.669093
O16	-0.712585	0.131879	-0.635126	-0.216183	-0.944088	-0.648781
O17	-0.547051	0.034074	-0.350884	-0.161655	-0.720530	-0.358468
O19	-0.985476	0.115891	-1.119642	-0.378849	-1.388873	-1.147531
O20	-4.652023	0.176057	-4.324439	0.038416	-4.744142	-4.445781
O21	-1.234367	0.141809	N/A	-0.185787	-1.456213	N/A
O22	-0.415065	0.077167	-0.643822	-0.315925	-0.743071	-0.662562
O23	-0.312865	N/A	-0.289709	-0.300249	-0.620852	-0.296875

using skew-derived drift rates, and c) corrected using OCloC's weighted least-squares estimates of the drift rates and the initial clock errors. Before correction, the later lapse cross-correlations shift monotonically to an earlier time (Figure 11a). The skew-derived corrections shift the lapse cross-correlations to later times. In this case, however, the skew-derived drift rate appears to "overcorrect" the lapse cross-correlations: later lapse cross-correlations now shift monotonically to a later time (Figure 11b). Finally, shifting the lapse cross-correlations using the weighted least-squares inversion for the a_i and b_i results in lapse cross-correlations that properly align (Figure 11c).

In Figure 11, the skew-derived drift and the drift recovered using the weighted least-squares inversion are compared for a single station couple only. In Figure 12, a more systematic and quantitative comparison of the linear drift based on our code ('OCloC-drift') and the skew values ('skew-drift') is presented for three OBSs. The drifts of all the other OBSs are shown in Appendix C. Figure 12 also shows the time offsets between the lapse cross-correlations and a reference lapse cross-correlation (RCF). We only use the cross-correlations between the OBSs and land stations. For each station pair, the highest signal-to-noise ratio cross-correlation is selected as the RCF. The time offsets correspond to the time shift that maximizes the Pearson correlation coefficient between the RCF and each cross-correlation. The skew-derived drift in the top figures assumes that there is no initial clock error at the onset of deployment (i.e., $b = 0$), and all subsequent time offsets are linearly interpolated based on this assumption. For the bottom figures, the time offset at deployment time corresponds to
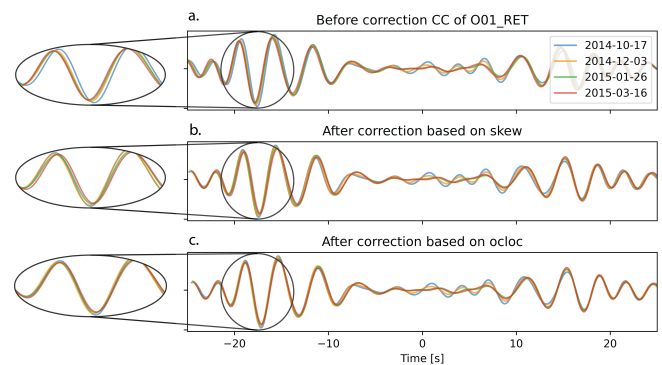

Figure 11 Lapse cross-correlations between OBS O01 and land-station RET in the frequency range of 0.2 to 0.4 Hz. Colors indicate the average time of all time windows that contribute to the lapse cross-correlation, and this color scheme is consistent across all three sub-figures (legend provided in the upper right corner of figure a). a. Original lapse cross-correlations prior to any corrections. b. Lapse cross-correlations after clock drift correction using skew values. c. Lapse cross-correlations after clock drift correction using the (OCloC-derived) drift rates (a_i) and initial clock errors (the b_i) estimated in this study.

the OBS' b value (or initial clock error) estimated from the weighted least-squares inversion (again, all subsequent offset times are interpolated accordingly).

The OCloC-drift corrections of OBS01 and OBS02 (Figures 12a and 12b) seem to align better with the time offset between the cross-correlations and the RCF. This is not the case for OBS10 (Figure 12c), where the skew-based clock drift aligns better with the time offsets. Sta-

tion O10, however, is also one of the stations with the shortest recording time, which results in fewer time-lapses. This highlights one limitation of our approach: the need for longer monitoring time to include more lapse cross-correlations, because that provides tighter constraints for the inversion process. In Section 5.3, we further discuss the implications of the OBSs not monitoring for a full year.

4.2 Comparing inversion strategies

The fact that a non-uniform illumination pattern can break the time symmetry of the retrieved surface-wave responses is detrimental to the method presented in this study. Weemstra et al. (2021) showed that applying a weighted least-squares inversion based on station-to-station distances decreases the adverse effects of a non-uniform surface wave illumination. Using synthetic recordings of ambient seismic noise, these authors demonstrated the advantage of the weighted least-squares estimate over the ordinary least-squares estimate. To evaluate the accuracy of the weighted least-squares estimator $\tilde{\mathbf{t}}_{(\mathrm{wls})}^{(\mathrm{ins})}$ in the presence of a non-uniform surface wave illumination, we compare it to the ordinary least-squares estimator $\tilde{\mathbf{t}}_{(\mathrm{ols})}^{(\mathrm{ins})}$. To do so, we used the bootstrap re-sampling approach introduced in Section 3.4. Figure 13 shows the histogram and cumulative distribution of 1000 bootstrap realizations of the a^* values of both inverse strategies. We used the same starting parameters and data vectors in both cases. The weighted inversions are shown in red, whereas the ordinary least-squares inversions are shown in blue. Figure 13a shows the distribution of the bootstrap realizations for all stations centered around 0 (mean values have been subtracted for each OBS individually). Figure 13b shows the cumulative distribution of the bootstrap realizations, with the 5th and 95th quantiles marked as vertical lines. The weighted least-squares distribution has narrower confidence intervals than the ordinary least-squares distribution.

For data vectors associated with large station-to-station distance thresholds, we do not find significant differences between both inversion strategies. This is expected because the threshold removes measurements associated with station couples that are closer to each other, which hence removes those lapse cross-correlations that are susceptible to larger illumination-related noise errors. For data vectors resulting from decreasing station-to-station distance thresholds, however, we find that the weighted inversion results in narrower bootstrap confidence intervals.

5 Discussion

5.1 The effect of the surface wave (noise) illumination pattern

A limitation of the presented method is the fact that a non-uniform illumination pattern can lead to deviations of the retrieved surface-wave responses from the true surface-wave responses (e.g., Tsai, 2009; Weaver
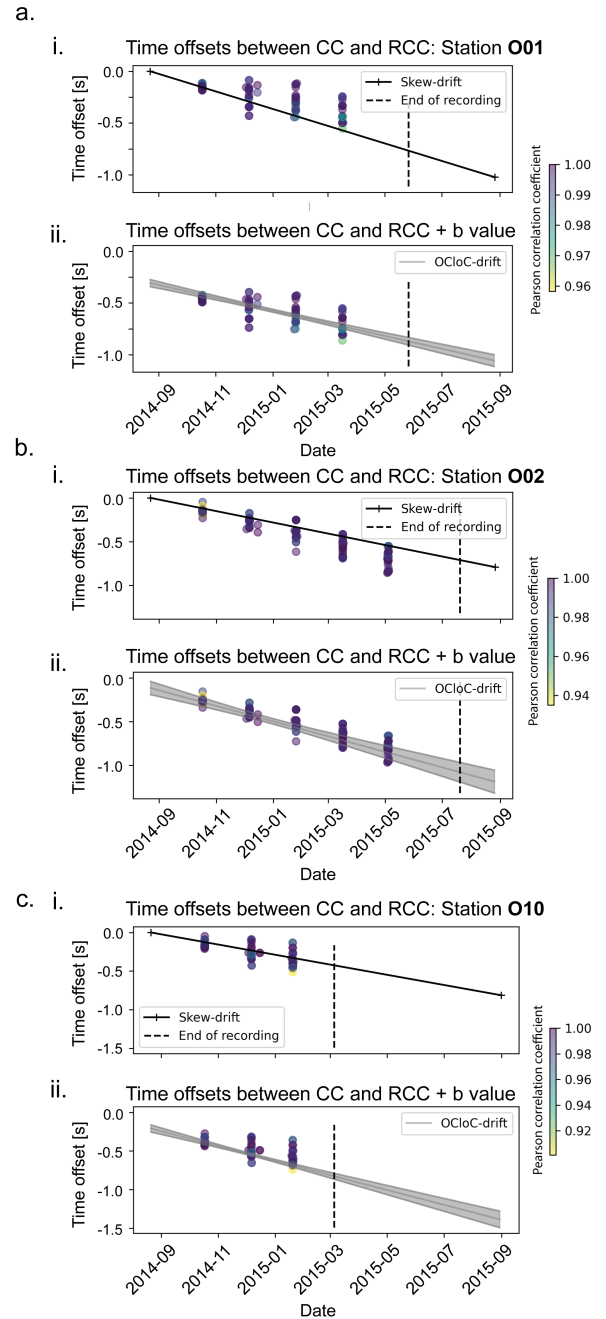

Figure 12 Comparison between (i) the skew-derived linear clock drift and (ii) the linear clock drift recovered using the weighted least-squares inversion for three selected OBSs. **Top**: Time offsets between cross-correlations and a reference cross-correlation (RCF) assuming no initial clock error at the onset of deployment. **Bottom**: Time offsets considering the initial clock error (b value) at deployment time. The drift based on our code (weighted least-squares inversion) and the confidence intervals are dubbed 'OCloC-drift', while the drift based on the skew values is termed 'skew-drift'. The highest signal-to-noise ratio cross-correlation for each station pair is chosen as the RCF. The depicted time offsets result from maximizing the Pearson correlation coefficient between the RCF and the other lapse cross-correlations, plus a correction based on the b value to the skew correction.

et al., 2009). As such, timing errors due to a non-uniform illumination pattern (captured in $\mathbf{n}^{(\mathrm{src})}$) lead
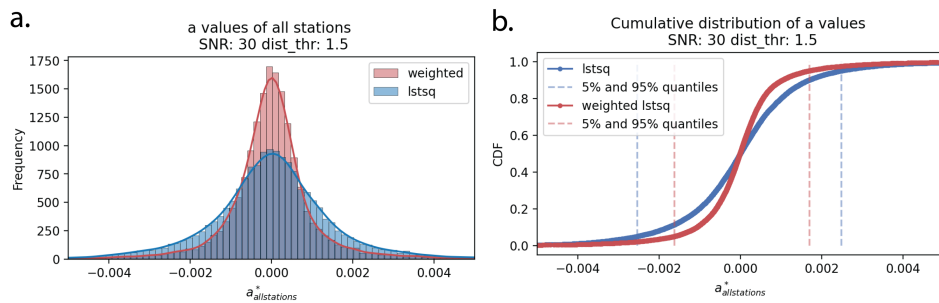
Figure 13 Bootstrap analysis of a^* values for all stations showing the 1000 realizations stacked for all stations. The mean values have been removed. The results of the weighted least-squares inversion are shown in red, and the results of the ordinary least-squares inversion are depicted in blue. a. Frequency histogram of the recovered values for all stations, with the probability density function overlaid. b. Cumulative distribution of the bootstrap realizations, with the 5th and 95th quantiles marked.

to deviations of the recovered drift from the true clock drift. Consequently, bootstrap confidence intervals can be expected to be larger for more pronounced non-uniform illumination patterns. The bootstrapping results presented in Section 4.2 show that the distance-based weighted least-squares inversion result in both a lower spread of the distribution of the a^* values (Figure 13a) and a narrower range between the 5th and 95th quantiles (Figure 13b).

The bootstrapping results presented in Section 4.2 confirm the earlier, synthetic-data-based findings by Weemstra et al. (2021). Compared to the ordinary least-squares inversion, the weighted least-squares inversion decreases the adverse effects of a non-uniform illumination pattern. Note that the reasoning above can also be turned around: the fact that the weighted least-squares inversion results in more accurate clock drift estimates strongly suggests a (time-varying) non-uniform surface wave illumination. Given the available literature (Stehly et al., 2006; Mulargia, 2012; Weemstra et al., 2013) in general, and the large differences in SNRs between (some of) the causal and acausal direct surface waves in particular, this can hardly be surprising.

5.2   Validation using only land stations

We run a separate test using only the lapse cross-correlations between the land stations. Lapse cross-correlations involving OBSs are discarded. Apart from two stations, we pretend these land stations to be suffering from clock errors and hence neither eliminate the columns associated with any of them from **A** (in reality, those stations' a and b coincide with zero of course) nor any of its two entries from $\mathbf{t}^{(\mathrm{ins})}$. We subsequently compute the weighted least-squares estimator of $\mathbf{t}^{(\mathrm{ins})}$. The inversion yields drift rates (i.e., a_i) of maximum 0.1 s/year, which demonstrates that (i) noise on the data (i.e., non-zero $\mathbf{n}^{(\mathrm{src})}$ and $\mathbf{n}^{(\mathrm{spur})}$) prevents the recovery of drift rates of 0 s/day and (ii) that drift rates lower than 10^{-4} s/day cannot be recovered unambiguously (for our specific station configuration, noise illumination, and frequency band). The maximum b_i that is recovered has a value of 0.12 s, but this is an outlier in the sense that for most of the stations, the estimated initial clock error at $t^{(\mathrm{lps})} = 0$ does not exceed 0.05 s. Although the recov-

ered a_i and b_i do not coincide with zero, we know that, in practice, the land stations do not suffer from clock drift and/or initial clock errors. Effectively, this experiment tells us that our approach allows us to successfully recover a seismic station's clock drift with an uncertainty of approximately 0.1 s/year.

5.3   On the validity of the assumption of linear clock drift and an initial clock error

While introducing our model (Section 2.2), we assumed the clock drift rates to be constant. Specifically, we formulated a time-dependent clock error $\delta t_i^{(\mathrm{ins})}(t^{(\mathrm{lps})})$ which drifts at a constant rate a_i, while allowing for a possible clock error b_i at $t^{(\mathrm{lps})} = 0$. The latter is introduced to allow for an initial clock error at deployment time. This could, for example, be invoked by the temperature shock while the OBS is sunk (Zhang et al., 2023). We discuss in this section (i) the differences between the skew-derived drift rates and the recovered drift rates (i.e., the a_i), (ii) the fact that the b_i are non-zero, and (iii) the relation between these two observations.

First, we would like to emphasize that the differences between the skew-derived drift rates and the parameters recovered using the weighted least-squares inversion (i.e., the a_i and b_i) yield clock errors at the time of recovery that differ at maximum 0.62 s (compare the last two columns of Table 1); most of them much less. This suggests that the skew values are rather representative of the clock drift of the OBSs at the time of recovery (see also Figure 10). Furthermore, Figure 12 and Appendix C preclude a decision as to which drift rate is "better" based on the time offsets of the consecutive lapse cross-correlations.

Second, Figure 12 and Appendix C also do not allow us to draw firm conclusions regarding the estimated initial clock errors at the onset of deployment (i.e., the b_i). Upon comparison with the time offsets between the individual lapse cross-correlations and the RCF, however, the clock errors estimated using our weighted least-squares inversion seem to be slightly more accurate than the skew-derived clock errors for most OBSs. This would confirm the existence of a (non-zero) initial clock error. For OBS O01, for example, the waveform align-

ment presented in Figure 11 strongly supports the estimated initial clock error (b) of -0.31 s. In particular because the estimated clock error at the time of recovery almost coincides with the skew for this station (see Table 1). By not taking into account the initial clock error for this OBS, the skew-based corrections effectively overcompensate the observed clock drift. This is evident from the shift of later lapse cross-correlations to positive times in Figure 11b. In contrast, OCloC-based corrections do not yield any (visible) residual drift (Figure 11c). This implies that an initial clock error at the time of deployment (i.e., a non-zero b) is indeed needed to explain the observed clock errors. Note that OBS O01 is used as an example because this station has one of the largest initial clock errors at deployment time, whereas its estimated clock error at recovery time almost coincides with the measured skew.

The fact that the OCloC-corrected lapse cross-correlations align better than the skew-corrected lapse cross-correlations can hardly be surprising. The drift rate estimates and the initial clock errors at the time of deployment are based on these very lapse cross-correlations. Therefore, it can be misleading to conclude from this observation that our approach yields more accurate drift rates than the skew-derived drift rates. This is because although the weighted least-squares inversion mitigates the effect of arrival time shifts resulting from a non-uniform surface wave illumination, it will not undo it entirely. Illumination-related arrival time shifts (i.e., non-zero $\delta t_{i,j,k}^{(+,\text{src})}$) may still have some effect. However, given the fact that (i) we averaged hourly cross-correlations over a period of 100 days, (ii) an SNR-threshold of 30 was imposed, and (iii) a station-to-station separation threshold of 2.5 wavelengths needed to be exceeded, we do not expect that these illumination-related arrival time shifts to be the cause of b_i as high as 0.3 or 0.4 s. The experiment discussed in Section 5.2 supports this claim.

Considering the above, we identify two possible explanations for the fact that the initial clock errors at the time of deployment are found to be non-zero and have values as high as (minus) 0.4 s. One explanation is that they result from the temperature shock during the OBS' descent to the ocean floor (see e.g., Zhang et al., 2023). In other words, they are real. This would not be surprising considering the experimental results by Gardner and Collins (2012), who find that the drift rates of the SEASCAN clocks may change significantly in the weeks after a temperature shock (in practice: after deployment). A second possible explanation for their deviation from zero stems from the fact that the OBSs experience seasonal temperature variations during their deployment at (relatively) shallow depths. The study by Jochumsen et al. (2016), for example, reports on seasonal seawater-temperature variations on the order of five degrees centigrade at those depths. This is consistent with the temperature variations within the data logger, which reveal annual temperature variations of about four degrees centigrade (these temperature sensors have a resolution of one degree only). In general, an OBS' drift rate is temperature dependent (Shariat-Panahi et al., 2009). However, we do not expect the drift

rate of the SEASCAN clocks to suffer from such temperature variations: the SEASCAN clocks are temperature compensated (Gardner and Collins, 2012). Nonetheless, if such a seasonally varying drift would exist, it may be more appropriate to have our drift model (Equation 2) include a sinusoid with a period of one year. This may be the topic of future work.

Of all recovered drift rates, the drift rate by OBS O20 stands out (see Figure 10). This may well be explained by the fact that, compared to the other OBSs, the logger and hence SEASCAN crystal oscillator of OBS O20 was newer. It was only two years old at the time of deployment, whereas the loggers (and hence clocks) of the other OBSs were approximately 8 years old (Alfred Wegener Institute, personal communication, 2023). This matters because of a natural process in the crystal oscillator, which is referred to as aging. Aging implies that the drift rate of an oscillator slowly changes with time. Essentially, it is the time derivative of the drift rate (Gardner and Collins, 2012). The aging of the crystal is a very important factor when it comes to the drift rate of the SEASCAN clocks, with younger crystals usually aging faster. And even though aging can be mitigated by regular recalibration of the SEASCAN clocks, it could well have been the cause of the larger drift rate of the SEASCAN clock of OBS O20.

5.4 Performance in the absence of land stations?

OBS arrays in remote oceanic regions will not have the benefit of land stations in their near vicinity. In that case, lapse cross-correlations between the OBSs and a station with a correct (UTC) reference time do not contribute to the data vector $\mathbf{t}^{(\text{app})}$. The system of equations will, in that case, be underdetermined (the rank of $\mathbf{A}$ being lower than the number of unknowns) and that weighted least-squares estimator $\tilde{\mathbf{t}}_{(\text{wls})}^{(\text{ins})}$ is chosen that has the lowest norm (see Section 2.6). The minimum-norm solution yields an estimator of $\mathbf{t}^{(\text{ins})}$ that allows the OBS recordings to be synchronized with respect to each other, but not with respect to UTC. In other words, the recovered b_i differs from the true (unknown) b_i by a common time shift, but the drift rates (i.e., the a_i) can still be recovered (with some uncertainty, of course). This is still useful as it would enable tomographic studies using only the OBSs, or the localization of seismic events (earthquake hypocenters) below the OBS array.

The accuracy of the recovered clock drift parameters depends linearly on the wave frequency. That is, lapse cross-correlations at higher frequencies will hence result in more accurate estimates of clock drift than lapse cross-correlations at lower frequencies, provided the illumination pattern and the SNRs at both frequencies coincide. In practice, the latter is often not the case: lapse cross-correlations at lower frequencies usually benefit from more uniform noise illumination patterns (e.g., Yang and Ritzwoller, 2008). It may therefore be beneficial to include measurements associated with different frequency bands in $\mathbf{t}^{(\text{app})}$. It is beyond the scope of this work to investigate this here.

5.5   Which projects can benefit from OCloC?

There are several methods that can be used for correcting OBS clock errors. The fastest to implement is simply using the recovered skew values and assuming a linear drift rate. Here, however, we show that this method may not be reliable. Moreover, it may not be possible because the battery has died before recovery. Other methods require correcting each OBS one by one by simply evaluating cross-correlations of ambient seismic noise in a non-automated manner. This requires a level of inspection that is not attractive (time-wise) for large-N OBS arrays. OCloC is suitable for such type of deployment as it automatically and simultaneously computes clock drift rates of all OBSs. Other cases where a GPS clock is lost, particularly with only on-land-station deployments, can significantly benefit from OCloC.

Projects that do not benefit from our approach are those with a limited deployment time. The reason is that OCloC requires the retrieval of interferometric surface wave responses at positive and negative times. In addition, lapse cross-correlations need to be computed at different lapse times $t_k^{(\text{lps})}$ (at least two). To retrieve both responses, noise cross-correlations need to be averaged over a sufficiently long time. Here "sufficiently long" is location, processing, and frequency dependent (e.g., Yang and Ritzwoller, 2008; Seats et al., 2012; Snieder, 2004). In our case (Reykjanes peninsula, spectral whiting prior to cross-correlation, and 0.2–0.4 Hz frequency band), individual noise cross-correlations were averaged over 100 days to obtain surface waves with sufficiently high SNRs at both positive (causal peak) and negative (acausal peak) time.

For projects that might not be suitable for OCloC, alternative solutions exist, such as the methodologies proposed by Sens-Schönfelder (2008); Hable et al. (2018); Loviknes et al. (2020); Jousset et al. (2013); Gouédard et al. (2014), among others.

6   Conclusions

We introduced a new method to recover, simultaneously, clock drift rates of large numbers of ocean bottom seismometers. Our approach relies predominantly on the time-symmetry of the retrieved interferometric surface wave responses, but also includes the perceived temporal stability of the lapse cross-correlations in the workflow (see Appendix B). Contrary to existing approaches, our method also (i.e., in addition to the drift rate) allows one to recover an initial clock error at the time of deployment. Two situations can be distinguished: OBS deployments including land stations and OBS deployments without stations devoid of a clock error. Drift rates will successfully be recovered in both situations. The absolute time, however, will be meaningless in case no land station (or another station devoid of clock errors) is "connected" to OBS deployment by means of a number of lapse cross-correlations. Results can be analyzed using a qualitative uncertainty analysis via bootstrap re-sampling. Finally, the presented methodology is implemented in OCloC, an accessible Python package with an object-oriented design.

We test OCloC using the seismic noise data acquired during IMAGE's seismic campaign in and around the Reykjanes Peninsula (Iceland). We find that all OBSs in the network suffered from clock drift. In particular, we find that the skew did not allow accurate recovery of the OBSs' drift rates. Using our approach, it was possible to detect the OBSs' initial clock error at the time of deployment. Finally, we showed that a weighted least-squares inversion, where receiver pairs are weighted by station-to-station distances, significantly reduces errors caused by deviations of the noise illumination pattern from uniform.

7   Acknowledgments

Code availability

Name of the package: OCloC (OBS Clock Correction)
Contact: d.f.naranjohernandez@tudelft.nl
Program language: Python
The documentation can be found at: https://ocloc.readthedocs.io
The source codes are available for download at: https://github.com/davidn182/ocloc

Competing interests

The authors have no competing interests.

References

Aki, K. Space and time spectra of stationary stochastic waves, with special reference to microtremors. *Bulletin of the Earthquake Research Institute*, 35:415–456, 1957. doi: 10.15083/0000033938.

Blanck, H., Jousset, P., Hersir, G. P., Ágústsson, K., and Ólafur G. Flóvenz. Analysis of 2014–2015 on- and off-shore passive seismic data on the Reykjanes Peninsula, SW Iceland. *Journal of Volcanology and Geothermal Research*, 391:106548, 2020. doi: 10.1016/j.jvolgeores.2019.02.001.

Boschi, L. and Weemstra, C. Stationary-phase integrals in the cross correlation of ambient noise. *Reviews of Geophysics*, 53 (2):411–451, 2015. doi: 10.1002/2014RG000455.

Claerbout, J. F. Synthesis of a layered medium from its acoustic transmission response. *Geophysics*, 33(2):264–269, 1968. doi: 10.1190/1.1439927.

Dongmo Wamba, M., Montagner, J.-P., and Romanowicz, B. Imaging deep-mantle plumbing beneath La Réunion and Comores hot spots: Vertical plume conduits and horizontal ponding zones. *Science Advances*, 9(4):eade3723, Jan. 2023. doi: 10.1126/sciadv.ade3723.

Draganov, D., Wapenaar, K., Mulder, W., Singer, J., and Verdel, A. Retrieval of reflections from seismic background-noise measurements. *Geophysical Research Letters*, 34(4), 2007. doi: 10.1029/2006GL028735.

Efron, B. *The jackknife, the bootstrap and other resampling plans*. SIAM, 1982. doi: 10.1137/1.9781611970319.

Efron, B. *Bootstrap Methods: Another Look at the Jackknife*. Springer New York, New York, NY, 1992. doi: 10.1007/978-1-4612-4380-9_41.

Fichtner, A. Source and processing effects on noise correlations. *Geophysical Journal International*, 197(3):1527–1531, 2014. doi: 10.1093/gji/ggu093.

Froment, B., Campillo, M., Roux, P., Gouédard, P., Verdel, A., and Weaver, R. Estimation of the effect of nonisotropically distributed energy on the apparent arrival time in correlations. *Geophysics*, 75, 09 2010. doi: 10.1190/1.3483102.

Gardner, A. T. and Collins, J. A. Advancements in high-performance timing for long term underwater experiments: A comparison of chip scale atomic clocks to traditional microprocessor-compensated crystal oscillators. In *2012 Oceans*, pages 1–8, 2012. doi: 10.1109/OCEANS.2012.6404847.

Geissler, W. H., Matias, L., Stich, D., Carrilho, F., Jokat, W., Monna, S., IbenBrahim, A., Mancilla, F., Gutscher, M.-A., Sallarès, V., and Zitellini, N. Focal mechanisms for sub-crustal earthquakes in the Gulf of Cadiz from a dense OBS deployment. *Geophysical Research Letters*, 37(18), 2010. doi: 10.1029/2010GL044289.

Gouédard, P., Seher, T., McGuire, J., Collins, J., and Hilst, R. D. Correction of Ocean-Bottom Seismometer Instrumental Clock Errors Using Ambient Seismic Noise. *Bulletin of the Seismological Society of America*, 104:1276–1288, 2014. doi: 10.1785/0120130157.

Groos, J., Bussat, S., and Ritter, J. Performance of different processing schemes in seismic noise cross-correlations. *Geophysical Journal International*, 188(2):498–512, feb 2012. doi: 10.1111/j.1365-246X.2011.05288.x.

Hable, S., Sigloch, K., Barruol, G., Stähler, S. C., and Hadziioannou, C. Clock errors in land and ocean bottom seismograms: high-accuracy estimates from multiple-component noise cross-correlations. *Geophysical Journal International*, 214 (3):2014–2034, 06 2018. doi: 10.1093/gji/ggy236.

Halliday, D. and Curtis, A. Seismic interferometry, surface waves and source distribution. *Geophysical Journal International*, 175 (3):1067–1087, 12 2008. doi: 10.1111/j.1365-246X.2008.03918.x.

Hannemann, K., Krueger, F., and Dahm, T. Measuring of clock drift rates and static time offsets of ocean bottom stations by means of ambient noise. *Geophysical Journal International*, 196: 1034–1042, 02 2014. doi: 10.1093/gji/ggt434.

Harris, C. R., Millman, K. J., van der Walt, S. J., Gommers, R., Virtanen, P., Cournapeau, D., Wieser, E., Taylor, J., Berg, S., Smith, N. J., Kern, R., Picus, M., Hoyer, S., van Kerkwijk, M. H., Brett, M., Haldane, A., Fernández del Río, J., Wiebe, M., Peterson, P., Gérard-Marchant, P., Sheppard, K., Reddy, T., Weckesser, W., Abbasi, H., Gohlke, C., and Oliphant, T. E. Array programming with NumPy. *Nature*, 585:357–362, 2020. doi: 10.1038/s41586-020-2649-2.

Hunter, J. D. Matplotlib: A 2D Graphics Environment. *Computing in Science Engineering*, 9(3):90–95, 2007. doi: 10.1109/M-CSE.2007.55.

Jochumsen, K., Schnurr, S. M., and Quadfasel, D. Bottom temperature and salinity distribution and its variability around Iceland. *Deep Sea Research Part I: Oceanographic Research Papers*, 111: 79–90, 2016. doi: 10.1016/j.dsr.2016.02.009.

Jousset, P., Budi-Santoso, A., Jolly, A. D., Boichu, M., Surono, Dwiyono, S., Sumarti, S., Hidayati, S., and Thierry, P. Signs of magma ascent in LP and VLP seismic events and link to degassing: An example from the 2010 explosive eruption at Merapi volcano, Indonesia. *Journal of Volcanology and Geothermal Research*, 261: 171–192, 2013. doi: 10.1016/j.jvolgeores.2013.03.014.

Jousset, P., Blanck, H., Franke, S., Metz, M., Ágústsson, K., Verdel, A., Ryberg, T., Hersir, G., Weemstra, K., Bruhn, D., and Flovenz, O. "Seismic Tomography in Reykjanes , SW Iceland". In *European geothermal congress 2016*, pages 1–10, 2016. http://europeangeothermalcongress.eu/.

Jousset, P., Hersir, G. P., Blanck, H., Kirk, H., Erbas, K., Hensch, M., Franke, S., Bruhn, D., and Huenges, E. IMAGE (Integrated Methods for Advanced Geothermal Exploration). GFZ Data Services. Other/Seismic Network. 2020a. doi: 10.14470/9Y7569325908.

Jousset, P., Mortensen, A. K., Ómar Fridleifsson, G., Ágústsson, K., and Gudmundsson, M. T. Reykjanes, Iceland: Structure and dynamics of mid-oceanic ridge geo/hydrothermal systems. *Journal of Volcanology and Geothermal Research*, 391:106692, 2020b. doi: 10.1016/j.jvolgeores.2019.106692.

Krischer, L., Megies, T., Barsch, R., Beyreuther, M., Lecocq, T., Caudron, C., and Wassermann, J. ObsPy: A bridge for seismology into the scientific Python ecosystem. *Computational Science and Discovery*, 8:014003, 05 2015. doi: 10.1088/1749-4699/8/1/014003.

Lindner, F., Weemstra, C., Walter, F., and Hadziioannou, C. Towards monitoring the englacial fracture state using virtual-reflector seismology. *Geophysical Journal International*, 214(2):825–844, 04 2018. doi: 10.1093/gji/ggy156.

Lobkis, O. and Weaver, R. On the emergence of the Green's function in the correlations of a diffuse field. *Journal of the Acoustical Society of America*, 110(6):3011–3017, 2001. doi: 10.1121/1.1417528.

Loviknes, K., Jeddi, Z., Ottemöller, L., and Barreyre, T. When Clocks Are Not Working: OBS Time Correction. *Seismological Research Letters*, 91(4):2247–2258, 05 2020. doi: 10.1785/0220190342.

Matsumoto, H., Zampolli, M., Haralabus, G., Stanley, J., Mattila, J., and Meral Ozel, N. Interpretation of detections of volcanic activity at Ioto Island obtained from in situ seismometers and remote hydrophones of the International Monitoring System. *Scientific Reports*, 9:19519, 12 2019. doi: 10.1038/s41598-019-55918-w.

Mulargia, F. The seismic noise wavefield is not diffuse. *The Journal of the Acoustical Society of America*, 131(4):2853, 2012. doi: 10.1121/1.3689551.

Rücker, C., Günther, T., and Wagner, F. M. pyGIMLi: An open-source library for modelling and inversion in geophysics. *Computers and Geosciences*, 109:106–123, 2017. doi: 10.1016/j.cageo.2017.07.011.

Schnaidt, S. and Heinson, G. Bootstrap resampling as a tool for un-

certainty analysis in 2-D magnetotelluric inversion modelling. *Geophysical Journal International*, 203(1):92–106, 08 2015. doi: 10.1093/gji/ggv264.

Seats, K. J., Lawrence, J. F., and Prieto, G. A. Improved ambient noise correlation functions using Welch's method. *Geophysical Journal International*, 188(2):513–523, 2012. doi: 10.1111/j.1365-246X.2011.05263.x.

Sens-Schönfelder, C. Synchronizing seismic networks with ambient noise. *Geophysical Journal International*, 174(3):966–970, 09 2008. doi: 10.1111/j.1365-246X.2008.03842.x.

Shapiro, N. M. and Campillo, M. Emergence of broadband Rayleigh waves from correlations of the ambient seismic noise. *Geophysical Research Letters*, 31(7), 2004. doi: 10.1029/2004GL019491.

Shariat-Panahi, S., Alegria, F. C., Làzaro, A. M., and del Rio, J. Time Drift of Ocean Bottom Seismometers (Obs). In *Proceedings of the 19th IMEKO World Congress on Fundamental and Applied Metrology*, pages 2548–2553, 2009.

Snieder, R. Extracting the Green's function from the correlation of coda waves: A derivation based on stationary phase. *Phys. Rev. E*, 69:046610, Apr 2004. doi: 10.1103/PhysRevE.69.046610.

Stehly, L., Campillo, M., and Shapiro, N. M. A study of the seismic noise from its long-range correlation properties. *Journal of Geophysical Research: Solid Earth*, 111(B10), 2006. doi: 10.1029/2005JB004237.

Sánchez-Pastor, P., Obermann, A., Schimmel, M., Weemstra, C., Verdel, A., and Jousset, P. Short- and Long-Term Variations in the Reykjanes Geothermal Reservoir From Seismic Noise Interferometry. *Geophysical Research Letters*, 46(11):5788–5798, 2019. doi: 10.1029/2019GL082352.

Tary, J. B., Géli, L., Henry, P., Natalin, B., Gasperini, L., Çomoğlu, M., Çağatay, N., and Bardainne, T. Sea-Bottom Observations from the Western Escarpment of the Sea of Marmara. *Bulletin of the Seismological Society of America*, 101(2):775–791, 04 2011. doi: 10.1785/0120100014.

Tsai, V. C. On establishing the accuracy of noise tomography travel-time measurements in a realistic medium. *Geophysical Journal International*, 178(3):1555–1564, 2009. doi: 10.1111/j.1365-246X.2009.04239.x.

Wapenaar, K. and Fokkema, J. Green's function representations for seismic interferometry. *GEOPHYSICS*, 71(4):SI33–SI46, 2006. doi: 10.1190/1.2213955.

Warner, M. and Guasch, L. Adaptive Waveform Inversion - FWI Without Cycle Skipping - Theory. In *76th Conference and Exhibition, EAGE, Expanded Abstracts*. European Association of Geoscientists and Engineers, 2014. doi: 10.3997/2214-4609.20141092.

Weaver, R., Froment, B., and Campillo, M. On the correlation of non-isotropically distributed ballistic scalar diffuse waves. *The Journal of the Acoustical Society of America*, 126(4):1817–1826, 2009. doi: 10.1121/1.3203359.

Weemstra, C., Boschi, L., Goertz, A., and Artman, B. Seismic attenuation from recordings of ambient noise. *GEOPHYSICS*, 78(1): Q1–Q14, 2013. doi: 10.1190/geo2012-0132.1.

Weemstra, C., Westra, W., Snieder, R., and Boschi, L. On estimating attenuation from the amplitude of the spectrally whitened ambient seismic field. *Geophysical Journal International*, 197: 1770–1788, 2014. doi: 10.1093/gji/ggu088.

Weemstra, C., de Laat, J. I., Verdel, A., and Smets, P. Systematic recovery of instrumental timing and phase errors using interferometric surface-waves retrieved from large-N seismic arrays. *Geophysical Journal International*, 224(2):1028–1055, 10 2021. doi: 10.1093/gji/ggaa504.

Werthmüller, D., Rochlitz, R., Castillo-Reyes, O., and Heagy, L. Towards an open-source landscape for 3-D CSEM modelling. *Geophysical Journal International*, 227(1):644–659, 06 2021. doi: 10.1093/gji/ggab238.

Wes McKinney. Data Structures for Statistical Computing in Python. In Stéfan van der Walt and Jarrod Millman, editors, *Proceedings of the 9th Python in Science Conference*, pages 56 – 61, 2010a. doi: 10.25080/Majora-92bf1922-00a.

Wes McKinney. Data Structures for Statistical Computing in Python. In Stéfan van der Walt and Jarrod Millman, editors, *Proceedings of the 9th Python in Science Conference*, pages 56 – 61, 2010b. doi: 10.25080/Majora-92bf1922-00a.

Yang, Y. and Ritzwoller, M. H. Characteristics of ambient seismic noise as a source for surface wave tomography. *Geochemistry, Geophysics, Geosystems*, 9(2), 2008. doi: 10.1029/2007GC001814.

Zhang, J., Zhao, M., Yao, Y., and Qiu, X. Analysis of clock drift based on a three-dimensional controlled-source ocean bottom seismometer experiment. *Geophysical Prospecting*, 2023. doi: 10.1111/1365-2478.13384.

Appendices

A Matrix formulation

To clarify the rather mathematical description of the inverse problem, let's consider the following example. If one would compute monthly time-averaged cross-correlations for an OBS deployment of 10 stations that would last one full year, $N^{(\text{lps})}$ would be 12 and N (obviously) 10. This would imply the number of rows of the matrix $\mathbf{A}$ (and the length of the vectors $\mathbf{t}^{(\text{app})}$, $\mathbf{n}^{(\text{src})}$, and $\mathbf{n}^{(\text{spur})}$) would coincide with $12 \times (10 \times 9)/2 = 540$. The length of $\mathbf{t}^{(\text{ins})}$ would coincide with 20 (2×10) and so would the number of columns of $\mathbf{A}$. Expressing then $t_k^{(\text{lps})}$ in terms of days (instead of seconds, which is the customary unit of time) and setting it to zero at the onset of the OBS deployment, this would imply $t_1^{(\text{lps})} \approx 15$, $t_2^{(\text{lps})} \approx 46$, and so on, and so forth.

For N stations, vector $\mathbf{t}^{(\text{ins})}$ can be written as:

$$\mathbf{t}^{(\text{ins})} \equiv \begin{pmatrix} a_1 \\ b_1 \\ a_2 \\ b_2 \\ \vdots \\ a_N \\ b_N \end{pmatrix}, \tag{9}$$

To aid in the interpretation of Equation (8), we depict below (Figure 14) the rows associated with the first lapse cross-correlations (i.e., the lapse cross-correlations associated with $t_1^{(\text{lps})}$) are shown in light blue. In addition, we have depicted in purple (for $t_1^{(\text{lps})}$ only) the elements of the matrix associated with the lapse cross-correlation between stations 1 and 2, and in yellow the elements of the matrix associated with the lapse cross-correlation between stations 2 and 3. Note that, as it stands, the matrix in Figure 14 is rank deficient. This implies that the system of equations is underdetermined, and a unique solution does not exist. If one of the 10 stations is a

land station devoid of clock errors, the two columns associated with that station could be eliminated from $\mathbf{A}$ (that OBS' a and b would coincide with zero), and its two entries eliminated from $\mathbf{t}^{(\text{ins})}$. The resulting matrix $\mathbf{A}$ would be full rank, and a unique estimator of $\mathbf{t}^{(\text{ins})}$ would exist.
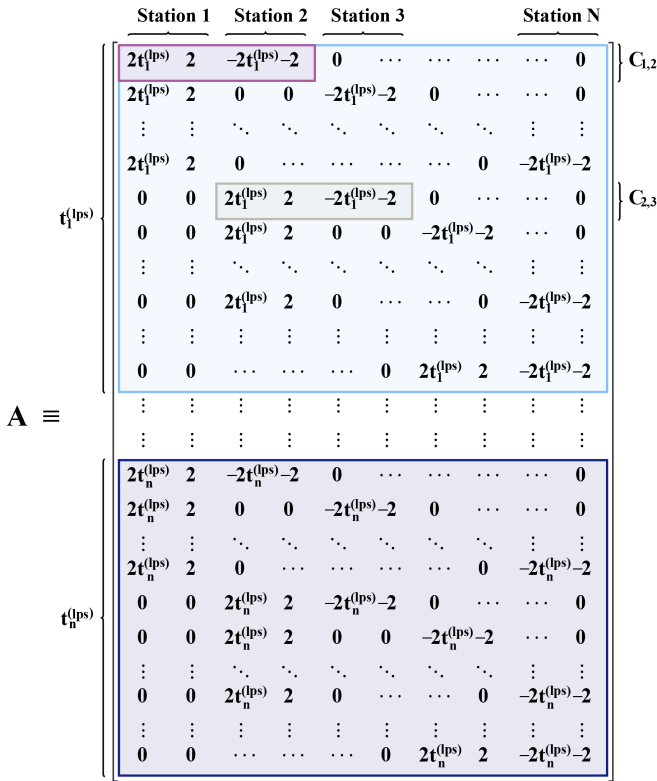
Figure 14 Example of matrix $\mathbf{A}$ when using N stations and n lapse times
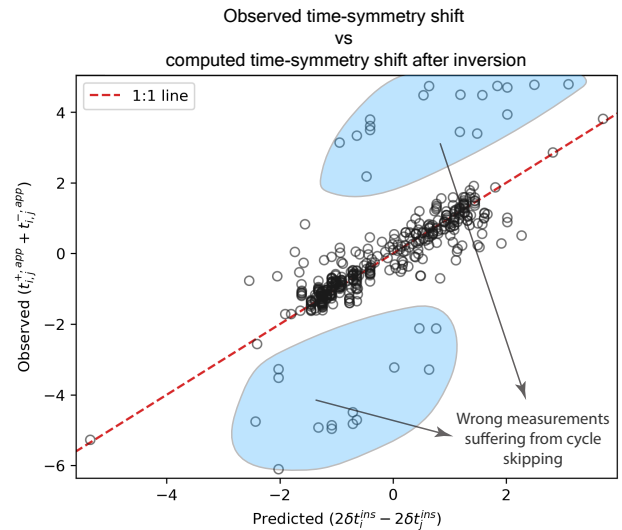
Figure 15 Observed time symmetry shifts plotted against the estimated time symmetry shifts after inversion. The clusters in blue might indicate inaccurate measurements product of cycle skipping.

skew values for each OBS. The figures display the time offsets between the cross-correlations and a chosen reference cross-correlation, offering a detailed view of our approach's alignment with standard skew value corrections across different OBSs. Stations with very high uncertainty (for example O03, O06, and O08) yielded fewer data points ($t_{i,j,k}^{+,app} + t_{i,j,k}^{-,app}$) as their SNR and distance separation did not meet the required thresholds (see Figure 6 for examples of those cross-correlations).

B   Detection of outliers

When measuring the $t_{i,j,k}^{(+,\text{app})} + t_{i,j,k}^{(-,\text{app})}$ it might be possible to get an erroneous measurement due to a phenomenon that is similar in nature to what is referred to as 'cycle skipping' in full-waveform inversion (e.g., Warner and Guasch, 2014). That is, the measured $t_{i,j,k}^{(+,\text{app})} + t_{i,j,k}^{(-,\text{app})}$ deviates from the "true value" by approximately one period (see also Weemstra et al., 2021). Needless to say, inclusion of these measurements in the inversion leads to incorrect a_i and b_i. To prevent such measurements, we implemented a method that compares the measured $t_{i,j,k}^{(+,\text{app})} + t_{i,j,k}^{(-,\text{app})}$ with the expected $t_{i,j,k}^{(+,\text{app})} + t_{i,j,k}^{(-,\text{app})}$. The latter is computed using the a's and b's recovered during a first inversion. After identifying the outliers, i.e., points that do not follow the overall trend (blue areas in Figure 15), we set a certain threshold for removing or keeping measurements. Repeating this process multiple times allows us to "clean" the data vector from such measurements.

C   Clock drifts of each OBS station

In this appendix section, we provide an extended comparison of linear corrections from our code against the
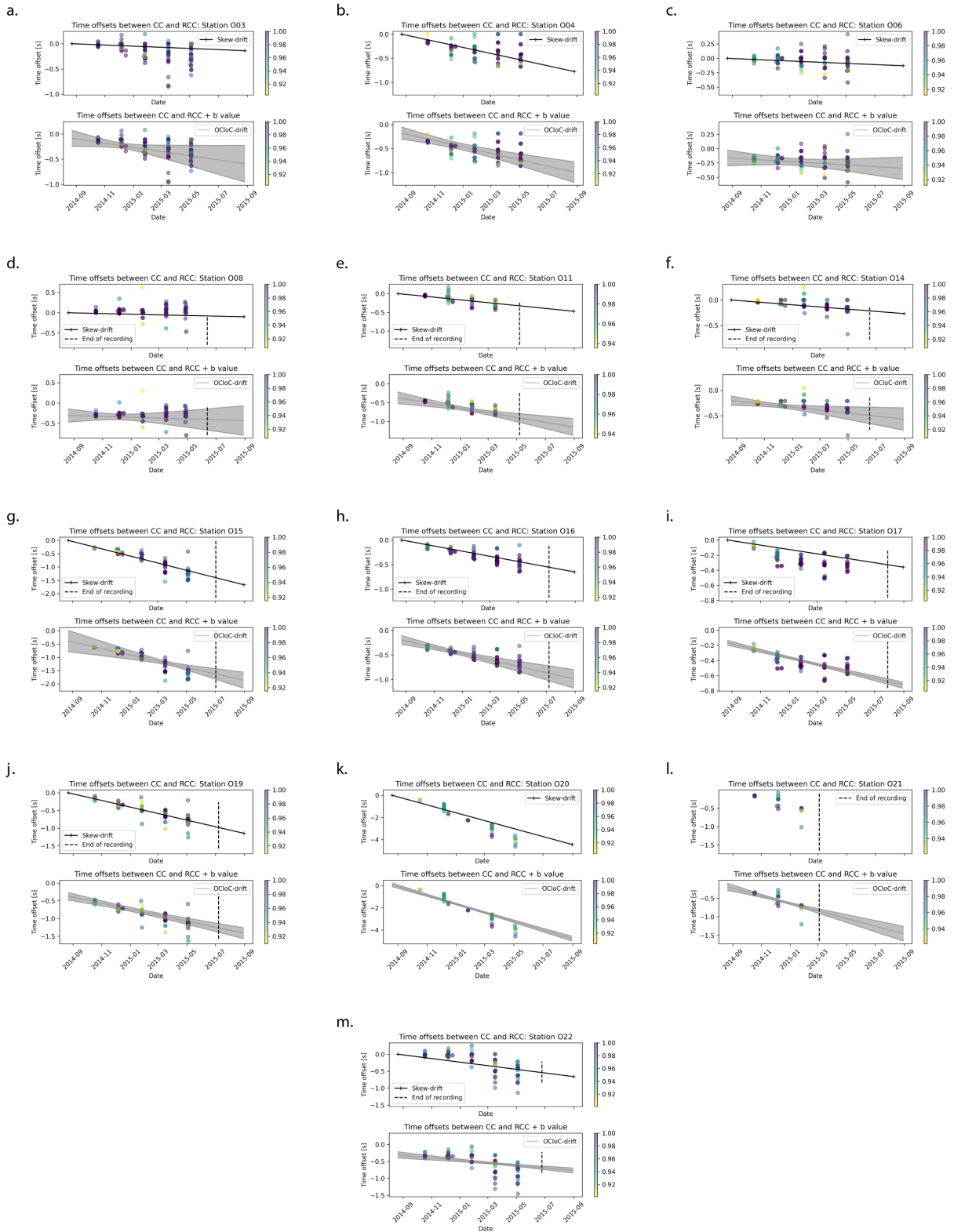
Figure 16 Comparison between the observed clock drift, (i) the skew-derived linear clock drift, and (ii) the linear clock drift recovered using the weighted least-squares inversion of each OBSs (except O01, O02, and O10, which are in Section 4). **Top**: Time offsets between cross-correlations and a reference cross-correlation (RCF) assuming no initial clock error at the onset of deployment. **Bottom**: Time offsets considering the initial clock error (b value) at deployment time. The drift based on our code (weighted least-squares inversion) and the confidence intervals is dubbed 'OCloC-drift', while the drift based on the skew values is termed 'skew- drift'. The highest signal-to-noise ratio cross-correlation for each station pair is chosen as the RCF. The depicted time offsets result from maximizing the Pearson correlation coefficient between the RCF and the other lapse cross-correlations, plus a correction based on the value of b in the skew correction.